Kinetic temperature of massive star-forming molecular clumps measured with formaldehyde

VI. The photodissociation region M17SW

X. Zhao[1,2], X. D. Tang[1,2,3], C. Henkel[4,1], K. M. Menten[4]⋆, Y. Gong[5], Y. Sun[5], Y. P. Ao[5], T. Liu[6], X. Lu[6], D. L. Li[1,2,3], Y. X. He[1,2,3], K. Wang[7], X. P. Chen[5], J. W. Wu[8,2], J. Esimbek[1,2,3], J. J. Zhou[1,2,3], X. W. Zheng[9], J. J. Qiu[10], J. S. Li[1,2], C. S. Luo[1,2], Q. Zhao[1,2], L. D. Liu[1,2], and C. Y. Wang[1,2]

1 State Key Laboratory of Radio Astronomy and Technology, Xinjiang Astronomical Observatory, CAS, Urumqi 830011, PR China
e-mail: tangxindi@xao.ac.cn
2 University of Chinese Academy of Sciences, Beijing 100080, PR China
3 Xinjiang Key Laboratory of Radio Astrophysics, Urumqi 830011, PR China
4 Max-Planck-Institut für Radioastronomie, Auf dem Hügel 69, 53121 Bonn, Germany
5 Purple Mountain Observatory, Chinese Academy of Sciences, Nanjing 210008, PR China
6 Shanghai Astronomical Observatory, Chinese Academy of Sciences, 80 Nandan Road, Shanghai 200030, PR China
7 Kavli Institute for Astronomy and Astrophysics, Peking University, Beijing 100871, PR China
8 National Astronomical Observatories, Chinese Academy of Sciences, Beijing 100101, PR China
9 School of Astronomy and Space Science, Nanjing University, Nanjing 210093, PR China
10 School of Mathmatics and Physics, Jinggangshan University, Ji'an 343009, PR China

July 10, 2026

ABSTRACT

The kinetic temperature structure of the photodissociation region M17SW was mapped using the IRAM 30 m telescope. This mapping employed the para-H_2CO triplet ($J_{K_aK_c} = 3_{03}–2_{02}$, $3_{22}–2_{21}$, and $3_{21}–2_{20}$) near 218 GHz on a scale of ~0.2 pc. The kinetic temperatures were derived by modeling the average H_2CO line ratios ($3_{22}–2_{21}/3_{03}–2_{02} + 3_{21}–2_{20}/3_{03}–2_{02}$) with the RADEX non-local thermodynamic equilibrium approach. These temperatures range from 28 to 181 K with an average of 54.2 ± 0.3 K at a spatial density of $5.5{\times}10^5$ cm^{-3}. Comparing with the temperature measurements obtained from multiple transitions of NH_3 (1,1)–(6,6) and the far-infrared (FIR) dust continuum, the H_2CO lines show temperatures similar to those measured by NH_3 but slightly higher than values derived from FIR observations. The high kinetic temperatures observed from H_2CO are associated with the ultracompact H II region UC1, dense clumps, and H_2O and CH_3OH masers, showing a similar distribution as NH_3. This indicates that dense gas in the M17SW region is heated by star formation activity. The presence of a significant gas temperature gradient across the M17SW region, as measured by H_2CO and NH_3, provides direct evidence for gas heated predominantly by radiation emitted from the OB star cluster NGC 6618. On a smaller scale, the dense gas surrounding the dense clumps experiences significant heating from internal protostars and/or young stellar objects. Higher temperatures traced by H_2CO are linked to turbulence on a scale of ~0.2 pc. The complex temperature structure of the M17SW region is revealed by H_2CO and NH_3, which may be attributed to both large-scale external radiative heating and small-scale internal radiative and turbulent heating.

Key words. stars: formation – stars: massive – ISM: clouds – ISM: molecules – radio lines: ISM

1. Introduction

The physical properties of the interstellar medium (ISM) significantly influence the star formation rate, spatial distribution, and fundamental characteristics of subsequent generations of stars, including their initial mass function and the elemental composition (e.g., Paumard et al. 2006; Kennicutt 1998a,b; Klessen et al. 2007; Papadopoulos et al. 2011; Zhang et al. 2018, 2025; Tang et al. 2019; Beuther et al. 2025; Gong et al. 2025). Massive stars play a crucial role in shaping their environments and influencing subsequent star formation through feedback such as outflows, stellar winds, ultraviolet (UV) radiation, and gas compression by expanding H II regions. However, the details of the massive star formation process and the ways in which their feedback modifies the initial conditions for massive stars remain inadequately understood. Radiative and mechanical interactions between massive stars and molecular clouds are fundamental for understanding galaxy evolution. Massive stars influence the evolution of molecular clouds by eroding and photo-evaporating their surfaces through intense UV radiation fields (e.g., Hernández-Vera et al. 2023; Gong et al. 2026). Additionally, UV radiation plays a crucial role in establishing the thermal gas pressure within star-forming clouds, with effects that can extend across various spatial scales, from the edges of molecular clouds to entire star-forming galaxies. Due to their powerful radiation fields and stellar winds, massive stars can either trigger or suppress the formation of new stars by compressing or disrupting their natal clouds (e.g., Elmegreen & Lada 1977; Walch et al. 2012; Kim et al. 2018b; Pabst et al. 2019; Luisi et al. 2021; Hernández-Vera et al. 2023). Therefore, it is essential to study the physical conditions of molecular clouds exposed to stellar UV radiation fields, par-

⋆ In memoriam.

Article published by EDP Sciences, to be cited as https://doi.org/10.1051/0004-6361/202659755

ticularly in the context of photodissociation or photo-dominated regions (PDRs), to evaluate the effects of stellar feedback. The thermal balance of the gas in such regions is governed by a combination of radiative and turbulent heating processes. In PDRs and cloud surfaces, the photoelectric effect on dust grains is the dominant radiative heating mechanism (e.g., Bakes & Tielens 1994; Weingartner & Draine 2001), followed by the photodissociation of H_2 and its UV pumping (e.g., Hollenbach et al. 1991; Girichidis et al. 2020). In denser regions, dust grains heated by the ambient radiation field transfer energy to the gas particles through collisions, efficiently coupling the dust and gas temperatures. Turbulent heating, on the other hand, arises from the dissipation of supersonic turbulence through shocks (e.g., Güsten & Fiebig 1988; Pan & Padoan 2009; Ao et al. 2013).

M17, also known as the Omega Nebula, is one of the most extensively studied young, active massive star-forming regions and ranks among the brightest H II regions in the sky (Lada et al. 1974; Hanson et al. 1997). Within this H II region lies the young open cluster NGC 6618, which comprises approximately 100 OB stars (Beetz et al. 1976; Chini et al. 1980; Hanson et al. 1997; Chini et al. 2000; Hoffmeister et al. 2008). These stars contribute to the heating of the surrounding gas and ionization of the M17 region (Lada et al. 1991; Hoffmeister et al. 2006). NGC 6618 has physically segmented the infrared structure of M17 into two distinct areas: M17 North and M17 South (Lada et al. 1991; Lada 1976). In the southwestern portion of M17, a compact molecular cloud known as M17SW has been identified. Extensive observations indicate that M17SW is one of the most representative PDRs in the Milky Way (Wilson et al. 1999; Brogan & Troland 2001; Pellegrini et al. 2007), with a distance of ∼2 kpc (Xu et al. 2011). The molecular cloud M17SW is situated adjacent to the H II region within M17, prompting extensive studies of M17SW as a PDR across high-energy, optical, infrared, and radio wavelengths (e.g., Felli et al. 1984; Mundy et al. 1987; Stutzki et al. 1988; Hobson 1992; Hobson et al. 1993; Jiang et al. 2002; Chen et al. 2012, 2013; Tang et al. 2013, 2014; Lim et al. 2020; Liu et al. 2022; Yanza et al. 2022; Zhu et al. 2023; Zhao et al. 2026). The heating and compression effects from the adjacent H II region may induce the collapse of the M17SW region, potentially leading to the formation of a new generation of stars. This makes M17SW a prime observational site for studying star formation processes (e.g., Chini et al. 1980; Lemke & Harris 1981; Felli et al. 1984; Stutzki & Güsten 1990; Hanson et al. 1997; Nielbock et al. 2001; Reid & Wilson 2006; Pérez-Beaupuits et al. 2012; Chen et al. 2021, 2025; Yin et al. 2022; Zhou et al. 2024).

The thermal structure of the M17SW region has been a subject of extensive study (see Appendix A for a synthesis of previous results). Previous observations indicate that the M17SW region is deeply influenced by the UV radiation from the H II region, resulting in a decreasing temperature trend away from the radiating source, and the direction is from northeast to southwest (e.g., Gatley et al. 1979; Thronson & Lada 1983; Harris et al. 1987; Stutzki et al. 1988; Güsten & Fiebig 1988; Stutzki & Güsten 1990; Greaves et al. 1992; Meixner et al. 1992; Bergin et al. 1994; Pérez-Beaupuits et al. 2010). Specifically, the dense molecular gas and dust at the interface between the H II region and the molecular cloud are heated primarily by UV radiation from the external OB cluster NGC 6618 (e.g., Gatley et al. 1979; Stutzki & Güsten 1990; Meixner et al. 1992). This external heating scenario has been further supported by subsequent molecular line and infrared continuum studies (e.g., Pérez-Beaupuits et al. 2010; Nishimura et al. 2018; Hoang et al. 2022). Evidence of dense gas being heated by turbulence in the M17SW region was discovered by Güsten & Fiebig (1988) through measurements using NH_3 on a scale of approximately 0.4 pc.

These studies provide valuable insights into the various layers of molecular clouds and the gas and dust temperature variations within the PDR of M17SW at different spatial scales. However, these studies are fundamentally limited by their angular resolutions. This lack of resolving power introduces significant uncertainty regarding the small-scale physics; the observed gradient could represent a smooth trend or be composed of discrete, unresolved temperature fluctuations. Consequently, comprehensive observations detailing the temperature of dense gas related to star formation in the M17SW region, particularly at a subparsec scale and with high resolution, remain lacking. Therefore, further research and high-resolution observations of M17SW are essential for a complete characterization of the thermal properties of dense gas.

Formaldehyde (H_2CO) is a ubiquitous molecule in the ISM, and its abundance remains stable across various evolutionary stages of star-forming regions. Previous observations indicate that the abundance of H_2CO does not vary by more than an order of magnitude throughout different stages of star formation (e.g., Mangum et al. 1990; Mangum & Wootten 1993; Caselli et al. 1993; Johnstone et al. 2003; Gerner et al. 2014; Tang et al. 2017a,b, 2018b; Liu et al. 2020; Gong et al. 2023). H_2CO exhibits numerous spectral transitions, ranging from centimeter to submillimeter wavelengths, and extensive observational studies demonstrate that its spectral lines can be employed to trace the physical properties of molecular clouds (e.g., Henkel et al. 1980, 1983; Mangum & Wootten 1993; Mangum et al. 2008, 2013, 2019; Ginsburg et al. 2011, 2016; Ao et al. 2013; Tang et al. 2017a,b, 2018a,b, 2021; Immer et al. 2016; Zhao et al. 2024). The relative populations of the K_a ladders of H_2CO are primarily governed by collisions, making the ratios of H_2CO line fluxes involving different K_a ladders effective indicators of temperature (Mangum & Wootten 1993; Tang et al. 2018b; Mazumdar et al. 2022; Kahle et al. 2023). The ratios of those H_2CO transitions have been utilized to measure the temperature of dense gas in various contexts, including Galactic star formation regions (e.g., Mangum et al. 1990; Mangum & Wootten 1993; Caselli et al. 1993; Johnstone et al. 2003; Gerner et al. 2014; Tang et al. 2017a,b, 2018b; Liu et al. 2020; Khan et al. 2026), the Galactic center (Qin et al. 2008; Ao et al. 2013; Johnston et al. 2014; Ginsburg et al. 2016; Immer et al. 2016; Lu et al. 2017; Zhang et al. 2025; Yue et al. 2026), and external galaxies (Mühle et al. 2007; Tang et al. 2017b, 2021; Mangum et al. 2019). Previous observations indicate that H_2CO is a sensitive tracer of dense gas in well-known Galactic PDRs, such as the Orion Bar, the Horsehead Nebula, and M8 (e.g., Leurini et al. 2010; Guzmán et al. 2011; Cuadrado et al. 2017; Tang et al. 2018a; Kahle et al. 2024). Additionally, H_2CO is useful in studying low-metallicity environments with strong UV radiation found in the Magellanic Clouds (e.g., Heikkilä et al. 1999; Wang et al. 2009; Tang et al. 2017b, 2021; Henkel et al. 2022). It is arguably one of the most effective molecular probes available for analyzing dense gas in PDRs. The distributions of multiple H_2CO spectral lines have been mapped in the M17SW region at low resolution (Lada & Chaisson 1975; Gardner & Whiteoak 1981; Mundy et al. 1987; Tang et al. 2013, 2014).

The main goal of this paper is to map the kinetic temperature ($T_{\rm kin}$) structure of the PDR M17SW at a scale of ∼0.2 pc by utilizing the para-H_2CO triplet ($J_{\rm K_aK_c} = 3_{03}$–2_{02}, 3_{22}–2_{21}, and 3_{21}–2_{20}), which has a critical density on the order of $n_{\rm crit}(H_2CO\ 3_{03}$–$2_{02}) \sim$ a few 10^5 cm^{-3} (Shirley 2015). We also aim to investigate the gas heating mechanisms affecting the dense gas in the con-

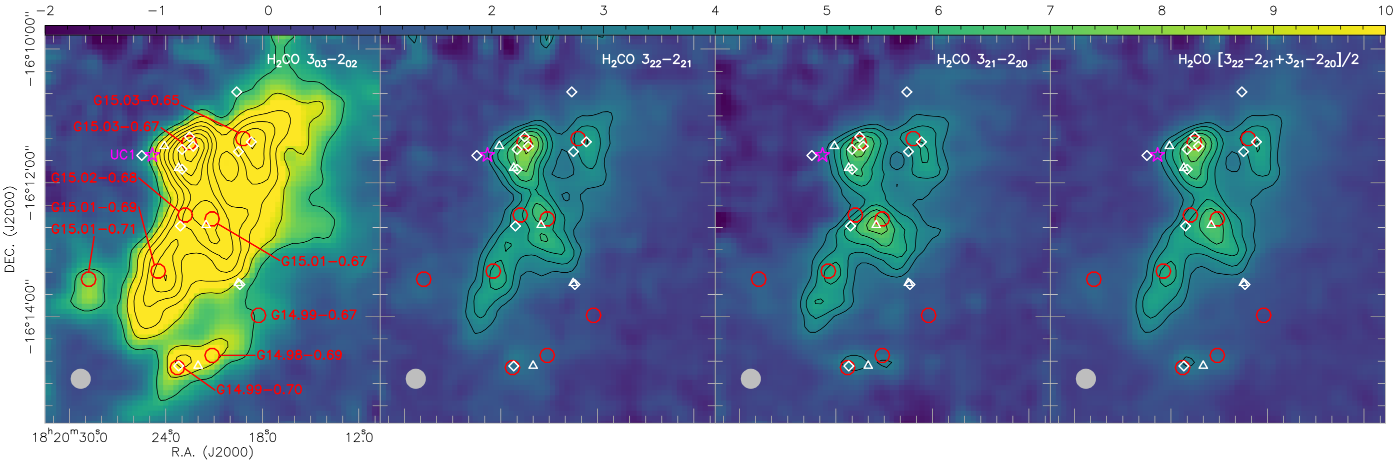

Fig. 1: Velocity-integrated intensity maps of H_2CO 3_{03}–2_{02} (*left*), 3_{22}–2_{21} (*mid-left*), 3_{21}–2_{20} (*mid-right*), and combined 3_{22}–2_{21} and 3_{21}–2_{20} (*right*) are shown on a $T_{\rm mb}$ scale, with the color bar in units of Kelvin kilometers per second. These maps are integrated over the velocity range of $V_{\rm LSR}$ = 14 to 26 km s^{-1} toward M17SW. Contour levels are from 6.0 to 27.0 K km s^{-1} with steps of 3.0 K km s^{-1} for H_2CO 3_{03}–2_{02}, and from 3 to 10 K km s^{-1} with steps of 1.0 K km s^{-1} for 3_{22}–2_{21}, 3_{21}–2_{20}, and combined 3_{22}–2_{21} and 3_{21}–2_{20}. The red circles represent the location of dense clumps identified from 850 μm continuum emission by Eden et al. (2019). The white diamonds and triangles and the magenta star indicate the locations of 22 GHz H_2O masers (Forster & Caswell 1999; Breen et al. 2010; Breen & Ellingsen 2011; Urquhart et al. 2011), Class I CH_3OH masers (Kurtz et al. 2004; Gómez et al. 2010; Kim et al. 2018a; Yang et al. 2020, 2023), and the ultracompact H II region UC1 (Felli et al. 1984), respectively. The beam size of each image is shown in the lower left corner.

text of star formation. The structure of the paper is as follows: In Sects. 2 and 3, we present our observations of the H_2CO triplet, data reduction, and results. The resulting kinetic temperatures derived from H_2CO are discussed in Sect. 4. Finally, we summarize our main conclusions in Sect. 5. This paper is part of the "Kinetic temperature of massive star-forming molecular clumps measured with formaldehyde" series of studies exploiting H_2CO as a probe of gas conditions in a variety of Galactic and extragalactic sources.

2. Observations and data reduction

We used the 9 dual-polarization pixel HEterodyne Receiver Array (HERA, Schuster et al. 2004) of the IRAM 30 m telescope[1] during May 2017 and October 2018 to map the M17SW molecular cloud. The H_2CO triplet ($J_{\rm K_aK_c}$ = 3_{03}–2_{02}, 3_{22}–2_{21}, and 3_{21}–2_{20}) transitions have rest frequencies of 218.222, 218.475, and 218.760 GHz, respectively. The central frequency was set to 218.475 GHz to ensure simultaneous measurements of all three lines. Within ∼1 GHz bandwidth, the backend spectrometer has 5377 channels, with each channel having a width of ∼0.27 km s^{-1}. The main beam size at ∼218 GHz is about 12″. The linear scale is ∼0.12 pc at a distance of 2 kpc. The main beam efficiency and the forward hemisphere efficiency[2] are 0.60 and 0.94, respectively. The observations were performed in the on-the-fly (OTF) model and were centered on α_{2000} = 18$^{\rm h}$20$^{\rm m}$21$^{\rm s}$.1 and δ_{2000} = -16°11′35″.7. Four ∼3 × 3 arcmin^2 maps were measured with steps of 3.5″ in both right ascension and declination, and the mapped area is ∼4.7 × 5.1 arcmin^2 (∼2.7 × 2.9 pc^2).

Data were reduced with GILDAS[3]. To enhance the signal-to-noise ratio (S/N) in individual channels, we smoothed three adjacent spectral channel, to a velocity resolution ∼0.8 km s^{-1}. The OTF maps were smoothed to a spatial resolution of 18″ and a 6″ grid using a Gaussian convolution kernel with inverse variance weighting. The comprehensive dataset comprising 5413 individual data points, each one corresponding to a distinct spectrum including various transitions. The detection rate was ∼41% for H_2CO 3_{03}–2_{02}, and ∼23% for the H_2CO 3_{22}–2_{21} and 3_{21}–2_{20} lines, each exhibiting S/N of ≳3σ. All H_2CO spectra with S/Ns above 3σ were fit by Gaussians. A typical rms noise level (1σ) of H_2CO 3_{03}–2_{02} is ∼0.12 K ($T_{\rm mb}$ scale) at a velocity resolution of ∼0.8 km s^{-1}.

The H_2CO 3_{22}–2_{21} and 3_{21}–2_{20} transitions exhibit analogous distributions and line profiles (brightness temperature, line width, and velocity in our observations; see Fig. 1), analogous to the situation in other star forming regions (e.g., Mangum & Wootten 1993; Tang et al. 2017a,b, 2018a,b, 2021; Zhao et al. 2024; Zhang et al. 2025). They belong to the same $K_{\rm a}$ ladder, and the energies between the ground state and these excited states are almost identical, $E_{\rm u}$ ≃ 68 K. Typically, H_2CO 3_{03}–2_{02} shows stronger emissions than H_2CO 3_{22}–2_{21} and 3_{21}–2_{20}. Furthermore, the line ratios of H_2CO 3_{22}–2_{21}/3_{03}–2_{02} and 3_{21}–2_{20}/3_{03}–2_{02} demonstrate analogous behaviors to probe the kinetic temperature of dense gas (Mangum & Wootten 1993; Tang et al. 2017a). Hence, we combined the line intensities of the two transitions channel by channel to further improve the S/Ns of H_2CO 3_{22}–2_{21} and 3_{21}–2_{20}.

The H_2CO 3_{03}–2_{02} spectral lines reveal multiple distinct velocity components at certain locations within the M17SW molecular cloud. These multiple velocity components originate in the northern edge of M17SW and sequentially connect through G15.03-0.65, G15.01-0.67, G15.02-0.68, and the region around G14.98–0.69 (see Fig. 1). We combined the data from these two velocity components based on their integrated intensities ratio (details see Sect. 3.5). Therefore, the gas temperature in positions with dual velocity components was not measured separately. Other positions were modeled using a single Gaussian.

[1] Based on observations obtained with the IRAM 30 m telescope. IRAM is supported by INSU/CNRS (France), MPG (Germany), and IGN (Spain).
[2] https://publicwiki.iram.es/Iram30mEfficiencies
[3] http://www.iram.fr/IRAMFR/GILDAS

The resultant line width measurements may be overestimated in these regions.

3. Results

3.1. Overview

The velocity-integrated intensity distributions of the H_2CO triplet and the combined $H_2CO\,3_{22}$–2_{21} and 3_{21}–2_{20} lines in the PDR M17SW ($V_{LSR} = 14$ to $26\,km\,s^{-1}$) are depicted in Fig. 1. Figures 2 and B.1 display the intensity-weighted velocity field (moment 1), line width (moment 2), and channel maps of $H_2CO\,3_{03}$–2_{02}. The observed H_2CO spectra of nine dense clumps, identified by 850 μm continuum emission (Eden et al. 2019) are illustrated in Fig. 3. The positions were converted to offset coordinates relative to our phase center at $\alpha_{2000} = 18^h20^m21\overset{s}{.}1$ and $\delta_{2000} = -16°11'35\overset{''}{.}7$. These positions were then registered to the nearest pixel in our data cube to ensure alignment with our observational grid. The locations of these dense clumps in M17SW are marked in Fig. 1 and detailed in Table 1. Table 1 also presents the parameters of the Gaussian fits for these dense clumps, encompassing velocity-integrated intensity ($\int T_{mb}\,dv$), local standard of rest velocity (V_{LSR}), full width at half maximum (FWHM) line width, and peak temperature (T_{mb}) of the H_2CO spectra.

3.2. Distribution of H_2CO

The $H_2CO\,3_{03}$–2_{02} velocity integrated intensity map shows the extensive distribution and provides a clear clumpy dense structure of M17SW (see the top left panel of Fig. 1). The strong H_2CO emission is consistent with the dense dust clumps (Eden et al. 2019). The spatial distribution of $H_2CO\,3_{03}$–2_{02} also closely aligns with previous observational results utilizing other gas tracers, such as $C^{18}O$ (2–1) and CO (6–5 and 7–6) (Stutzki & Güsten 1990; Pérez-Beaupuits et al. 2010), as well as dust emission at wavelengths of 450–850 μm (e.g., Hobson et al. 1993; Chen et al. 2025). In contrast, $H_2CO\,3_{22}$–2_{21} and 3_{21}–2_{20} exhibit more localized distributions, primarily detectable in the densest regions of M17SW, as depicted in the top right and bottom two panels of Fig. 1.

The intensity-weighted velocity (moment 1) and channel maps of H_2CO (3_{03}–2_{02}) elucidate the intricate velocity field within M17SW, as depicted in Figs. 2 and B.1. Velocity components ranging from approximately 20 to 23 $km\,s^{-1}$ are discernible at specific locations, including the clump G15.01-0.71, the eastern periphery of clump G15.02-0.68, clump G15.03-0.65 and its southern extended region, the connecting bridge between clumps G15.03-0.67 and G15.03-0.65, and the northwestern sector of M17SW. Additionally, velocity components within the range of approximately 16 to 18 $km\,s^{-1}$ are observed in the northern and southern sectors of M17SW. Notably, the eastern dense region of the primary structure of M17SW exhibits a velocity of around 19 $km\,s^{-1}$.

The line width distribution (moment 2) is illustrated in the bottom panel of Fig. 2. It is evident that regions exhibiting high line widths, exceeding approximately 3 $km\,s^{-1}$, are closely linked to dense clumps, specifically G15.03-0.67, G15.03-0.65, G15.02-0.68, G15.01-0.67, and G15.01-0.69. Moderate line widths (2–3 $km\,s^{-1}$) predominantly encircle the dense clumps within M17SW, while lower line widths ($\lesssim 2\,km\,s^{-1}$) are observed at the periphery of the primary structure of M17SW and at clump G15.01-0.71. The fit line width values for $H_2CO\,3_{03}$–2_{02} range from 1.2 to 7.5 $km\,s^{-1}$, with an average value of $3.8\pm0.1\,km\,s^{-1}$ (errors reported represent standard deviations of the mean). Approximately 34% of spectra with high line widths ($\geq 3\,km\,s^{-1}$) exhibit dual velocity components in the fit data, while this proportion is 53% for those with moderate line widths (2–3 $km\,s^{-1}$).

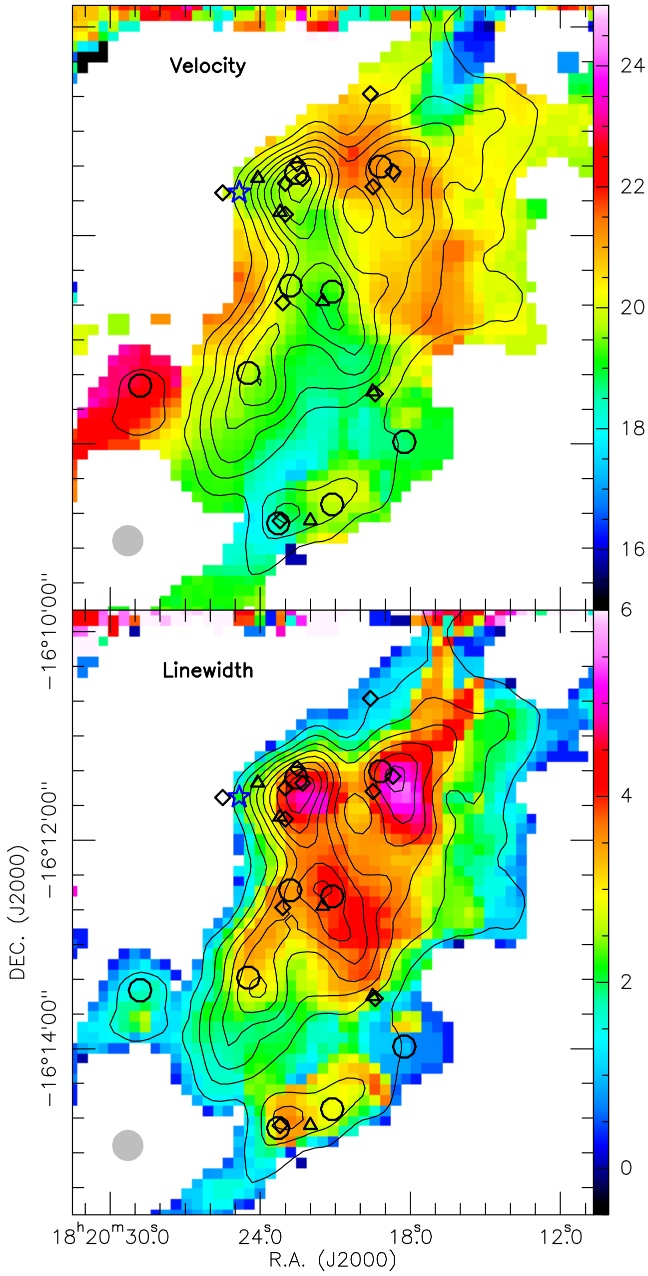

Fig. 2: Intensity-weighted velocity field (moment 1, *top*) and line width (moment 2, *bottom*) of $H_2CO\,3_{03}$–2_{02} are presented. The unit of each color bar is kilometers per second. Black contours show the integrated intensity of $H_2CO\,3_{03}$–2_{02} (same as in Fig. 1). The symbols are the same as Fig. 1.

3.3. H_2CO line ratios

As mentioned in Sect. 2, the line ratios $H_2CO\,3_{22}$–$2_{21}/3_{03}$–2_{02} and 3_{21}–$2_{20}/3_{03}$–2_{02} demonstrate similar patterns in determining the kinetic temperature of dense gas (e.g., Mangum & Wootten 1993; Tang et al. 2017a). In this work, we therefore utilize the average ratio of $H_2CO\,0.5\times[(3_{22}$–$2_{21} + 3_{21}$–$2_{20})/3_{03}$–$2_{02}]$ derived

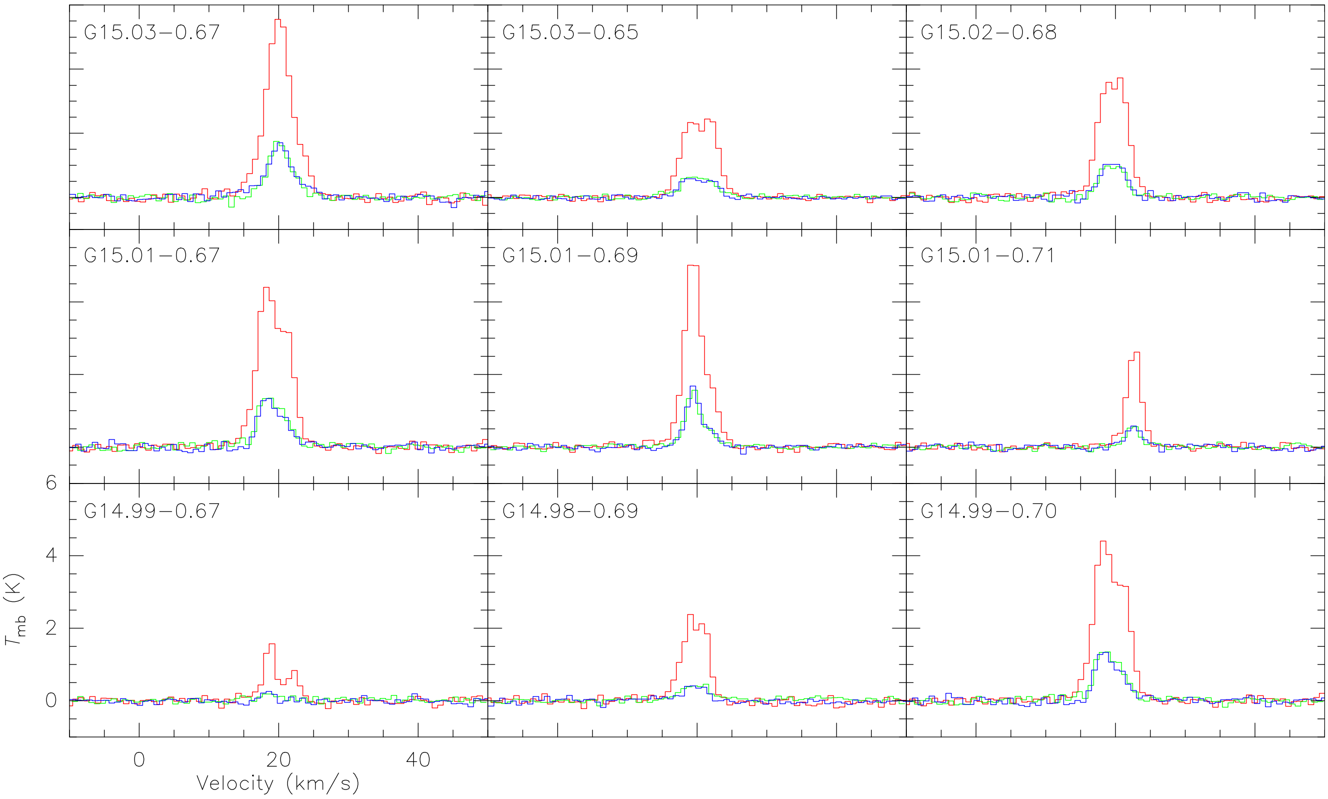

Fig. 3: Observed H_2CO spectra of the dense clumps in M17SW. Red, green, and blue lines show H_2CO 3_{03}–2_{02}, 3_{21}–2_{20}, and 3_{22}–2_{21}, respectively. The dense clumps were identified from 850 μm continuum emission by Eden et al. (2019) (details see Sect. 3.1 and Table 1).

Table 1: Parameters of the dense clumps in M17SW.

Clump	Offset	Transition	$\int T_{mb}\,dv$	V_{LSR}	FWHM	T_{mb}	σ_T	σ_{NT}	c_s	$\mathcal{M}$	T_{kin}	T^b_{dust}
	″ , ″		K km s^{-1}	km s^{-1}	km s^{-1}	K	km s^{-1}	km s^{-1}	km s^{-1}		K	K
G15.03-0.67	18, 12	3_{03}–2_{02}	26.4 (0.3)	20.0 (0.1)	4.6 (0.1)	5.4	0.14 (0.01)	1.96 (0.03)	0.50 (0.01)	4.0	71 (3)	35.9
		(3_{21}–2_{20}+3_{22}–2_{21})/2	7.5 (0.1)	20.0 (0.1)	4.4 (0.1)	1.6						
G15.03-0.65	–30, 18	3_{03}–2_{02}	20.2 (0.2)	21.1 (0.1)	6.3 (0.1)	3.0	0.12 (0.01)	2.67 (0.03)	0.44 (0.01)	6.1	55 (2)	32.7
		(3_{21}–2_{20}+3_{22}–2_{21})/2	4.9 (0.1)	20.9 (0.1)	5.9 (0.2)	0.8						
G15.02-0.68[a]	24, –54	3_{03}–2_{02}	18.8 (2.1)	19.7 (0.1)	2.9 (0.2)	6.2	0.13 (0.02)	1.21 (0.07)	0.45 (0.08)	2.7	58 (20)	–
		(3_{21}–2_{20}+3_{22}–2_{21})/2	4.7 (1.0)	19.4 (0.2)	2.6 (0.3)	1.7						
G15.01-0.67	0, –54	3_{03}–2_{02}	23.9 (0.2)	19.2 (0.1)	5.3 (0.1)	4.2	0.13 (0.01)	2.25 (0.03)	0.47 (0.01)	4.8	63 (3)	31.5
		(3_{21}–2_{20}+3_{22}–2_{21})/2	6.3 (0.2)	18.8 (0.1)	4.5 (0.1)	1.3						
G15.01-0.69	48, –102	3_{03}–2_{02}	18.4 (0.2)	19.6 (0.1)	3.6 (0.1)	4.9	0.13 (0.01)	1.51 (0.02)	0.47 (0.01)	3.2	62 (2)	–
		(3_{21}–2_{20}+3_{22}–2_{21})/2	4.8 (0.1)	19.4 (0.1)	3.1 (0.1)	1.4						
G15.01-0.71	108, –108	3_{03}–2_{02}	6.9 (0.1)	22.7 (0.1)	2.4 (0.1)	2.7	0.12 (0.01)	1.03 (0.02)	0.42 (0.02)	2.4	51 (4)	38.7
		(3_{21}–2_{20}+3_{22}–2_{21})/2	1.6 (0.1)	22.5 (0.1)	2.7 (0.2)	0.6						
G14.99-0.67	–42, –144	3_{03}–2_{02}	5.6 (0.2)	19.4 (0.1)	5.0 (0.3)	1.1	0.09 (0.01)	2.10 (0.12)	0.31 (0.01)	6.7	28 (2)	–
		(3_{21}–2_{20}+3_{22}–2_{21})/2	0.6 (0.1)	18.4 (0.2)	2.2 (0.4)	0.2						
G14.98-0.69[a]	0, –180	3_{03}–2_{02}	10.3 (0.7)	19.6 (0.1)	3.4 (0.2)	3.2	0.13 (0.02)	1.46 (0.09)	0.44 (0.06)	3.3	56 (17)	–
		(3_{21}–2_{20}+3_{22}–2_{21})/2	2.5 (0.4)	18.7 (0.5)	6.7 (1.1)	0.5						
G14.99-0.70	30, –192	3_{03}–2_{02}	12.0 (0.2)	18.2 (0.1)	5.9 (0.1)	1.9	0.12 (0.01)	2.52 (0.05)	0.43 (0.01)	5.9	53 (3)	–
		(3_{21}–2_{20}+3_{22}–2_{21})/2	2.8 (0.1)	18.0 (0.1)	6.4 (0.3)	0.4						

Notes. Offsets relative to our reference position for M17SW (see Sect. 3.1 and Fig. 1, Eden et al. 2019). The table also lists the velocity integrated intensity, $\int T_{mb}\,dv$, local standard of rest velocity, V_{LSR}, full width at half maximum line width (FWHM), and peak temperature (T_{mb}). These parameters were obtained from Gaussian fitting using CLASS as part of the GILDAS software package. For the thermal and nonthermal line widths, σ_T and σ_{NT}, the sound velocity c_s, the Mach number $\mathcal{M}$, the kinetic temperature T_{kin}, and the dust temperature T_{dust}, see Sects. 3 and 4.3. Values in parenthesis are 1σ uncertainties. [a] Clumps G15.02-0.68 and G14.98-0.69 are located in a region with two velocity components, their parameters are the combined values of both components (see Sect. 2). [b] The dust temperature taken from Urquhart et al. 2018.

from the combined H_2CO 3_{22}–2_{21} and 3_{21}–2_{20} to H_2CO 3_{03}–2_{02} velocity-integrated intensities as an indicator of the kinetic temperature. We selected the combined H_2CO 3_{22}–2_{21} and 3_{21}–2_{20} lines, which were detected at S/Ns above 3σ. Generally, higher H_2CO line ratios indicate elevated kinetic temperatures (Ao et al. 2013; Ginsburg et al. 2016; Tang et al. 2018a, 2021). Consequently, the ratio maps can serve as a proxy for the relative kinetic temperature. The line ratio map of H_2CO in M17SW is shown in the top left panel of Fig. 4. The line ratios range from 0.10 to 0.50 with an average value of 0.23 ± 0.01. Higher line ratios (> 0.3) are found at the eastern edge of the primary structure of M17SW, the edge of clump G15.01-0.71, clumps G15.03-0.67 and G14.99-0.70, the southern regions of clumps G15.03-0.65, G15.02-0.68, G15.01-0.67, and G15.01-0.69, as well as the

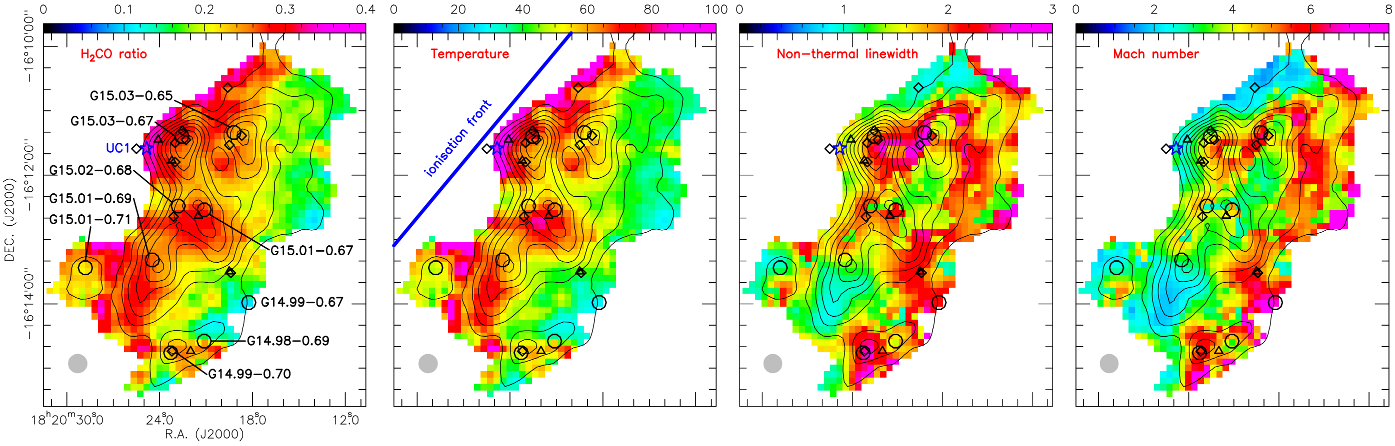

Fig. 4: Parameter maps of M17SW. *Left*: Averaged velocity-integrated intensity ratio map of H_2CO, calculated as 0.5×[(3_{22}–2_{21} + 3_{21}–2_{20})/3_{03}–2_{02}] (see Sect. 3.3). *Mid-left*: Kinetic temperatures derived from the H_2CO line ratios, represented by the color bar in units of Kelvin. The solid blue line indicates the location of the assumed ionization front. *Mid-right*: Map of nonthermal line width (color bar in units of km s^{-1}). *Right*: Map of Mach number. The black contours show the integrated intensity of H_2CO 3_{03}–2_{02} (same as in Fig. 1).

nearby ultracompact H II region UC1 and the H_2O and CH_3OH masers. Moderate line ratios ranging from 0.2 to 0.3 are observed widely spread in the periphery of the primary structure of M17SW. Lower line ratios (< 0.2) are found at the western edge of M17SW as well as the edges of clumps G15.01-0.71 and G14.99-0.70.

3.4. Kinetic temperatures derived from H_2CO line ratios

As previously mentioned, the determination of the kinetic temperature involves calculating the averaged ratio of H_2CO 0.5×[(3_{22}–2_{21} + 3_{21}–2_{20})/3_{03}–2_{02}]. To establish the relationship between the gas kinetic temperature and the observed average of H_2CO 0.5×[(3_{22}–2_{21} + 3_{21}–2_{20})/3_{03}–2_{02}] ratios, we employed the non-local thermodynamic equilibrium (LTE) model RADEX[4] (van der Tak et al. 2007) with collision rates obtained from Wiesenfeld & Faure (2013). In our analysis, we adopted a background temperature of 2.73 K, an average measured line width of 3.8 km s^{-1}, an H_2 number density of $n(H_2) = 5.5 \times 10^5$ cm^{-3}, and a para-H_2CO column density of N(para-H_2CO) = 6.5×10^{13} cm^{-2} in Fig. C.1. The corresponding volume and column densities were derived from the following analysis.

We assumed that the para-H_2CO (3–2) lines are optically thin in the M17SW region. The average H_2 volume density and H_2CO column density of the entire M17SW region were determined using multiple transitions of ortho-H_2CO (J = 2–1, 3–2, and 4–3) with an angular resolution of ~60″ (Mundy et al. 1987). The measured $n(H_2)$ ranged from $10^{4.3}$ to $10^{6.4}$ cm^{-3} with an average of 5.5×10^5 cm^{-3}, which is consistent with results obtained using CS and $C^{18}O$ (Mundy et al. 1986; Stutzki & Güsten 1990; Wang et al. 1993). We assumed that the para-H_2CO (3–2) lines observed originated from the same region with an average density of 5.5×10^5 cm^{-3} in the M17SW region as measured by Mundy et al. (1987). Furthermore, the derived N(ortho-H_2CO) ranges from $10^{13.4}$ to $10^{14.9}$ cm^{-2} with an average of 1.94×10^{14} cm^{-2} in the M17SW region (Mundy et al. 1987). Previous observations of H_2CO (J = 3–2 and 4–3) with the APEX 12 m telescope toward the dense clump G15.03-0.67 in M17SW indicated $n(H_2)$, N(para-H_2CO), and the ortho-to-para ratio of H_2CO to be 1.3×10^6 cm^{-3}, 6.2×10^{13} cm^{-2}, and ~3, respectively (Tang et al. 2018b). Based on these results, we assume the ortho-to-para ratio of H_2CO to be 3 in the entire M17SW region. Therefore, we calculated an average N(para-H_2CO) of 6.5×10^{13} cm^{-2} in the M17SW region based on previous measurements by Mundy et al. (1987). Using the methodology outlined in Sect. 3.1 of Tang et al. (2017b), we employed RADEX to recalculate the average column density N(para-H_2CO) of the entire M17SW region based on the H_2CO (3_{03}–2_{02}) average brightness temperature. The resulting value is approximately 4×10^{13} cm^{-2} at $n(H_2) = 5.5 \times 10^5$ cm^{-3}, which agrees well with the results obtained from Mundy et al. (1987). The H_2 column density derived from *Herschel* far-infrared (FIR) continuum data ranges from 1.0 to 4.0×10^{23} cm^{-2} with a median value of $\sim 2 \times 10^{23}$ cm^{-2} in the M17SW region (Hoang et al. 2022). Consequently, we calculated a typical fractional abundance of para-H_2CO to be approximately 3.3×10^{-10} in the M17SW region based on the above average column density of para-H_2CO. This result aligns with the typical observational value of $\sim 3.9 \times 10^{-10}$ at various evolutionary stages of star formation regions (Tang et al. 2018b). Therefore, the adopted average N(para-H_2CO) of the entire M17SW region is deemed reasonable in this study.

Previous observations regarding kinetic temperature have revealed subtle differences between various column densities at a given $n(H_2)$ (Tang et al. 2018b). In this study, we examine the relationship between kinetic temperature and the line ratios of para-H_2CO at N(para-H_2CO) values of 1.0, 6.5, and 13.0×10^{13} cm^{-2}, all at an $n(H_2)$ of 5.5×10^5 cm^{-3}, as illustrated in Fig. C.1. These comparisons highlight nuanced temperature variations across different column densities. The temperature differences derived from column densities of 1.0×10^{13} and 1.3×10^{14} cm^{-2}, in comparison to 6.5×10^{13} cm^{-2}, are found to be smaller than the uncertainties associated with temperature estimations based on line ratio measurements. Given the potential variability in the relationship between gas temperature and the H_2CO line ratio across different spatial densities, as illustrated in Fig. 4 of Tang et al. (2018b), we conducted modeling at spatial densities of 2×10^4 and 2.5×10^6 cm^{-3} based on previously measured $n(H_2)$ values (Mundy et al. 1987) using the RADEX. It appears that the T_{kin} measured at 5.5×10^5 cm^{-3} as utilized in this

[4] http://var.sron.nl/radex/radex.php

study exhibits a slight variation of less than 15% at spatial densities of 2×10^4 and 2.5×10^6 cm^{-3} for $T_{\rm kin}$ values below 100 K. Consequently, we could transform the line ratio map into a kinetic temperature map using a column density of 6.5×10^{13} cm^{-2} and an H_2 number density of 5.5×10^5 cm^{-3}. The maps showing the H_2CO line ratios and the corresponding kinetic temperatures derived from the H_2CO line ratios are presented in Fig. 4.

The validity of LTE as a dependable approximation for H_2CO level populations has been established under specific conditions, particularly when the relevant transitions are optically thin and the systems exhibit high densities (Mangum & Wootten 1993). Following the methodology described in Tang et al. (2017b) (refer to their Eq. (2)) and utilizing the RADEX model, we conducted a thorough analysis to explore the correlation between the kinetic temperature and the combined H_2CO line ratio within the LTE regime, as illustrated in Fig. C.1. It reveals a satisfactory agreement between the temperatures derived from the LTE model and those obtained from the RADEX model, assuming a column density of 6.5×10^{13} cm^{-2}, provided that $T_{\rm kin}$ remains below approximately 200 K.

The kinetic temperature in M17SW, as indicated by the H_2CO line ratios, ranges from 27 to 181 K, with an average value of 54.2 ± 0.3 K. The kinetic temperature map in Fig. 4 reveals that the highest temperature ($T_{\rm kin}$>100 K) is associated with UC1 and the eastern edge of M17SW. High temperatures (>70 K) are detected at the eastern edge of the primary structure of M17SW, the edge of clump G15.01-0.71, clumps G15.03-0.67 and G14.99-0.70, the southern regions of clumps G15.03-0.65, G15.02-0.68, G15.01-0.67, and G15.01-0.69, as well as near H_2O and CH_3OH masers. Moderate temperatures ranging from 50 to 70 K are widely observed in the periphery of the primary structure of M17SW. Lower temperatures (<50 K) are found at the western edge of M17SW and the edges of clumps G15.01-0.71 and G14.99-0.70.

Previous observations indicate that the H_2CO 3_{03}–2_{02} emission may be optically thick in the dense region (e.g., Immer et al. 2016; Tang et al. 2018b). This saturation could result in falsely high H_2CO 3_{22}–2_{21}/3_{03}–2_{02} and 3_{21}–2_{20}/3_{03}–2_{02} line ratios in our integrated intensity ratio map, potentially mimicking elevated gas temperatures in the clouds. As stated by Yue et al. (2026), the H_2CO (3–2) lines may overestimate the kinetic temperature when $T_{\rm kin}>100$ K. To address this issue, we utilized the RADEX non-LTE model to calculate the opacity of H_2CO 3_{03}–2_{02} line, adopting an average temperature of $T_{\rm kin}=54$ K, an average measured linewidth of 3.8 km s^{-1}, and a gas volume density of $n(H_2)=5.5\times10^5$ cm^{-3}. The para-H_2CO column density was taken as N(para-H_2CO) = 8.4×10^{12}–2.6×10^{14} cm^{-2}, derived from previous ortho-H_2CO measurements (Mundy et al. 1986) using an ortho-to-para ratio of 3 (Tang et al. 2018b). The resulting optical depths for the H_2CO 3_{03}–2_{02} line range from approximately 0.08 to 1.5. These values suggest that in the dense cores, opacities in the H_2CO 3_{03}–2_{02} lines may exhibit slight saturation, potentially leading to a minor overestimation of kinetic temperatures by less than 20%.

3.5. Thermal and nonthermal motions obtained from H_2CO

The thermal and nonthermal line widths (Pan & Padoan 2009; Dewangan et al. 2016) can be determined by the kinetic temperature obtained from the line ratios of H_2CO. We used $\sigma_{\rm T}=\sqrt{\frac{kT_{\rm kin}}{m_{\rm H_2CO}}}$ and $\sigma_{\rm NT}=\sqrt{\frac{\Delta v^2}{8\ln 2}-\sigma_{\rm T}^2}$ to calculate the thermal and nonthermal line widths in M17SW, respectively. In these formulas, k represents the Boltzmann constant, $T_{\rm kin}$ stands for the kinetic temperature of the gas, $m_{\rm H_2CO}$ denotes the mass of a formaldehyde molecule, and Δv indicates the measured FWHM line width of H_2CO 3_{03}–2_{02}. As outlined in Sect. 2, there are roughly 330 pixels (accounting for roughly 26%) exhibiting two velocity components at 18.5 and 21.5 km s^{-1}, aligning with previous findings from NH_3 and CO studies (Güsten & Fiebig 1988; Stutzki & Güsten 1990; Keown et al. 2019). Due to the proximity and low intensity of these two velocity components, neither the H_2CO 3_{22}–2_{21} and 3_{21}–2_{20} nor the combined 3_{22}–2_{21} and 3_{21}–2_{20} lines can effectively differentiate between the two velocity components. The precise determination of kinetic temperatures in regions characterized by dual velocity components presents challenges. Therefore, the line width is obtained as a weighted average of the line widths of the two velocity components within H_2CO 3_{03}–2_{02} based on their integrated intensities. The thermal line width ranges from 0.09 to 0.22 km s^{-1}, with an average value of 0.12 ± 0.01 km s^{-1}. Simultaneously, the nonthermal line width ranges from 0.87 to 3.2 km s^{-1}, with an average value of 1.67 ± 0.01 km s^{-1}. It is important to notice that the nonthermal line width surpasses the thermal line width. These results are consistent with previous H_2CO (J=3–2 and 4–3) observations of the massive star-forming regions in our Galaxy and Large Magellanic Cloud (Tang et al. 2017b, 2018a,b, 2021; Zhao et al. 2024).

The nonthermal line width distribution map of H_2CO 3_{03}–2_{02} is depicted in Fig. 4. This distribution is akin to the line width results observed in M17SW, with the exception of regions near the dense clumps G15.03-0.65, G15.01-067, and G15.02-0.68. As mentioned before, there are two velocity components in the central area of M17SW. In these specific locations, the nonthermal line width displays lower values, possibly due to the weighted average of the line widths of the two velocity components. The systematically lower $\sigma_{\rm NT}$ derived from two-component fits arises because the single-component alternative, when forced to fit a blended profile with a weak secondary peak, overestimates the line width by conflating the intrinsic turbulence with the unresolved velocity separation between components. Conversely, the nonthermal line width demonstrates higher values near clump G15.03-0.67, G15.03-0.65, G14.99-0.67, and G14.99-0.70, as well as along the northern and western edges of M17SW. This discrepancy could be attributed to the lower S/Ns of the spectral lines, rendering Gaussian profile fitting more challenging.

The Mach number ($\mathcal{M}=\sigma_{\rm NT}/c_{\rm s}$, in which $c_{\rm s}=\sqrt{\frac{kT_{\rm kin}}{\mu m_{\rm H}}}$, where $\mu=2.37$ is the mean molecular weight for molecular clouds and $m_{\rm H}$ is the mass of a hydrogen atom) distribution map of M17SW is shown in Fig. 4. The Mach number ranges from 1.3 to 8.5 with an average of 4.0 ± 0.1. This indicates that the dense gas in M17SW traced by H_2CO is dominated by supersonic nonthermal motions (e.g., turbulence, outflows, shocks). High Mach numbers ($\mathcal{M}>6$) are observed in the vicinity of the clumps G15.03-0.67, G15.03-0.65, G14.99-0.70, G14.99-0.67, and G14.98-0.69, as well as along the northern and western edges of M17SW. Medium Mach numbers ($4<\mathcal{M}<6$) are found to be associated with the dense clumps. Low Mach numbers ($\mathcal{M}<4$) are prevalent in the dense region of the primary structure and the eastern and southeastern edge of M17SW.

4. Discussion

4.1. Comparison of temperatures derived from gas and dust

As delineated in Appendix A and Table A.1, Güsten & Fiebig (1988) employed the Effelsberg 100 m telescope with a beam size of ∼ 40″ to conduct a temperature structure mapping of the M17SW region using multiple transitions of NH_3 (1,1)–(6,6). Their findings suggest that temperatures within the M17SW molecular cloud vary between approximately 30 and 275 K, with a bulk temperature of around 50 K. Approximately 10% of the gas populates the NH_3 (6,6) inversion transition level, which leads to a notably elevated measured temperature. Our temperature assessments derived from H_2CO (3–2) line ratios align closely with their reported outcomes. More recently, the temperature distributions of the M17SW region were also observed using NH_3 (1,1) and (2,2) with the GBT (beam size ∼32″, ∼0.32 pc; Keown et al. 2019). The temperature map derived from the NH_3 (2,2)/(1,1) line ratios is depicted in Fig. C.2 (also see Fig. 11 in Keown et al. 2019). The kinetic temperature of M17SW as determined from NH_3 (2,2)/(1,1) observations ranges from 20 to 80 K with an average of ∼40 K. Notably, temperatures exceeding 50 K are observed around the clumps G15.03-0.67, G15.03-0.65, and G15.01-0.71, while temperatures ranging from 30 to 40 K are prevalent around the clumps G15.02-0.68, G15.01-0.67, and G15.01-0.69. Lower temperatures of ∼20 K are identified in the clumps G14.99-0.67, G14.98-0.69, and G14.99-0.70. The temperature gradient derived from NH_3 in M17SW shows a decrease from east (>70 K) to west (∼20 K), displaying a similar distribution compared to the temperature distribution obtained from H_2CO (3–2) line ratios on a large scale. As mentioned in Sect. 3.4, the kinetic temperature derived from H_2CO near the ultracompact H II region UC1 reaches >100 K, and it decreases to about 30–40 K at the western edge of M17SW. The average temperature derived from NH_3 (2,2)/(1,1) line ratios of the M17SW region is slightly lower than that from the H_2CO (3–2) line ratios. The high kinetic temperatures obtained from H_2CO are associated with UC1, dense clumps, as well as H_2O and CH_3OH masers (see Sect. 3.4), displaying a similar distribution to NH_3. For the dense clumps G15.02-0.68, G15.01-0.67, G15.01-0.69, G14.98-0.69, and G14.99-0.70, the kinetic temperatures obtained from H_2CO show a different distribution compared to NH_3, all exhibiting significantly elevated temperatures from H_2CO relative to NH_3 (2,2)/(1,1). These observed differences may arise from the varying beam sizes of the two observations and/or the fact that higher-excitation H_2CO lines are more sensitive to warmer gas components. The energy levels of the H_2CO 3_{03}–2_{02}, 3_{22}–2_{21}, and 3_{21}–2_{20} lines are 21, 68, and 68 K, respectively, whereas NH_3 (1,1) and (2,2) exhibit E_u of 1 and 42 K. The elevated excitation energy of H_2CO renders it a more specific tracer of warm dense gas, as indicated by Ginsburg et al. (2016).

The CO observations from highly excited rotational levels (i.e., J = 7–6 and 14–13) reveal the presence of warm and dense gas in various regions of M17SW (Jaffe et al. 1987; Harris et al. 1987), with a complex molecular cloud structure surrounding the interface (Stutzki et al. 1988). Analysis of CO (J=7–6 and 14–13) and [OI] data indicates a kinetic temperature exceeding 200 K at the interface between the M17SW cloud and the OB star cluster (Harris et al. 1987; Stutzki et al. 1988), consistent with results obtained from H_2CO line ratios near UC1. Modeling of ^{13}CO J = 1–0 and 5–4 emissions reveals that the eastern edge of M17SW exhibits the highest gas temperature around 60 K, decreasing to ∼20 K at the western edge (Howe et al. 2000). These temperatures, while lower than those determined by H_2CO, are similar to those from NH_3 (2,2)/(1,1) measurements, all showing a consistent temperature gradient with H_2CO and NH_3. This suggests that the heating of the M17SW molecular cloud is influenced by external sources, particularly in the northeastern region where the OB star cluster is located.

As mentioned in Appendix A and Table. A.1, the dust temperature (T_{dust}) in the M17SW region has been investigated across various wavelengths ranging from 50 to 850 μm (e.g., Gatley et al. 1979; Meixner et al. 1992; Dupac et al. 2002; Hoang et al. 2022). These studies reveal that the typical dust temperature in the M17SW region falls within the range of approximately 20–120 K, akin to the gas temperatures derived from NH_3 (2,2)/(1,1) (Güsten & Fiebig 1988; Keown et al. 2019) and low-J ^{13}CO (Howe et al. 2000), albeit slightly lower than the values obtained from high-J CO (Harris et al. 1987; Stutzki et al. 1988) and H_2CO line ratios. This consistency aligns with previous findings in star-forming regions within our galaxy (e.g., Tang et al. 2017b, 2018a,b; Zhao et al. 2024). The dust temperature decreases from east to west within the M17SW cloud, with the highest dust temperature observed at the interface between the M17SW cloud and the OB stars (e.g., Harris et al. 1987; Güsten & Fiebig 1988; Stutzki et al. 1988; Meixner et al. 1992; Dupac et al. 2002; Hoang et al. 2022). This pattern mirrors the kinetic temperature distribution inferred from H_2CO line ratios and NH_3 on a larger scale, indicating a consistent heating effect from massive star clusters that is prominently visible in large-scale features.

4.2. Radiative heating

As discussed above, the M17SW molecular cloud is influenced by UV radiation emitted from OB star clusters in the northeast, leading to a temperature gradient that decreases from northeast to southwest within the cloud. To investigate the impact of external radiation on the heating of the M17SW molecular cloud, we analyzed the temperature profiles of H_2CO and NH_3 (see Fig. 5). The location of the "cavity" is considered to be the central point of the main source of the radiation source within the NGC 6618 open cluster (also see Fig. 13 in Lim et al. 2020), surrounded by the M17 H II region. This cavity, characterized by hot and diffuse mid-infrared and submillimeter emissions, as well as significant molecular line emission, is centered at $\alpha_{2000} = 18^h20^m31\overset{s}{.}2$ and δ_{2000} = -16°10′54″.8 (Townsley et al. 2003; Povich et al. 2007; Lim et al. 2020). Gas temperatures were obtained from measurements of H_2CO (3–2) and NH_3 (2,2)/(1,1) line ratios (Keown et al. 2019). For H_2CO data, the temperature uncertainties do not exceed 50% of the temperature value. Regarding NH_3 data, the S/Ns of NH_3 (2,2) are $\gtrsim$ 4 and the temperature errors are within 30% of the temperature value. Due to the limited reliability of high kinetic temperatures indicated by NH_3 (2,2)/(1,1) line ratios (e.g., Tang et al. 2017b, 2018a,b; Zhao et al. 2024), only NH_3 data with temperatures below 100 K were selected. As depicted in Fig. 5, the kinetic temperatures probed by H_2CO and NH_3 decrease noticeably with increasing projected distance (R) from the cavity. A power-law function is adopted here as an empirical description of the observed temperature decrease with distance. This form is scale-free, meaning it does not assume any characteristic length scale, and allows for a direct comparison with the theoretical curves derived from the Stefan-Boltzmann blackbody radiation law. Such a function has been widely applied to model temperature gradients in massive star-forming regions (e.g., Busquet et al. 2016; van 't Hoff et al. 2018; Tang et al. 2018a; Tobin et al. 2020; Gieser et al. 2021, 2022, 2023;

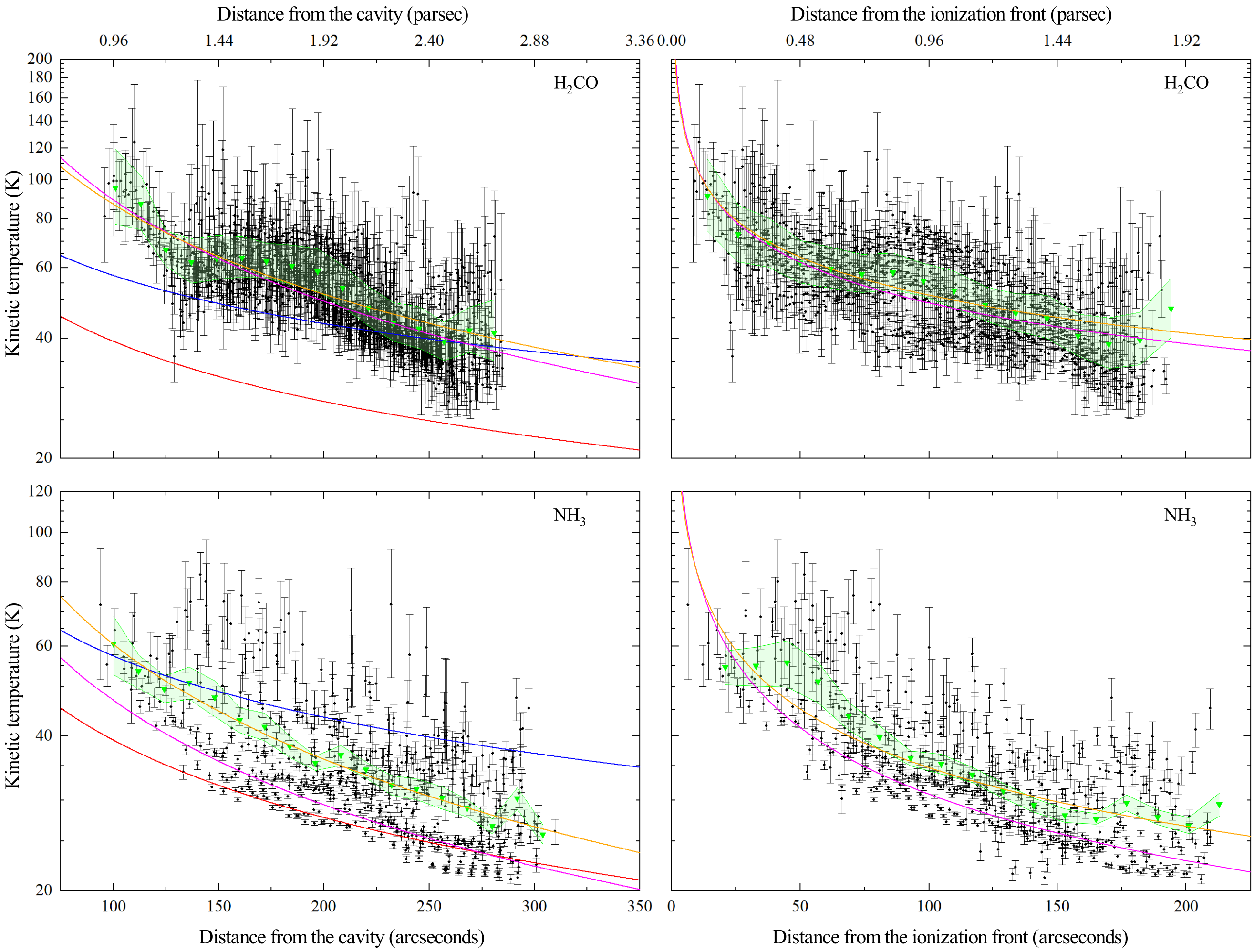

Fig. 5: Variation in kinetic temperature across the M17SW region with distance from the NGC 6618 cavity (*left panels*) and the assumed ionization front (*right panels*) (see Sect. 4.2). The kinetic temperatures are calculated from the line ratios of H_2CO (3–2) (*upper panels*) and NH_3 (2,2)/(1,1) (*lower panels*) (for details, see Sect. 4.2). The average kinetic temperature at each projected distance is denoted by green triangles within 12″ bins (∼0.12 pc), plotted at the bin centers, with the shaded green area representing the corresponding uncertainty. The magenta and orange lines represent the fit results for all data and binned data, respectively, with the regression equation formatted as $T_{\rm kin} = a \times (\frac{R}{\rm arcsec})^b$ K. The fitting method employed is the Levenberg-Marquardt algorithm, which accounts for temperature errors through instrumental weighting ($w = 1/\sigma^2$). The reduced Chi-squared values for all H_2CO and NH_3 data obtained from the cavity are 4.14 and 33.38, respectively. From the ionization front, these values are 5.79 and 25.21 for H_2CO and NH_3, respectively. For the binned data, the reduced Chi-squared values for H_2CO and NH_3 from the cavity are 0.34 and 0.73, while from the ionization front, they are 0.22 and 1.97, respectively. The red and blue lines depict the expected relationships derived from the Stefan-Boltzmann law and the modified Stefan-Boltzmann law, respectively.

Zhao et al. 2024). The fit results of H_2CO and NH_3 are

$$T_{\rm kin}({\rm H_2CO}) = 4413(\pm 487) \times \left(\frac{R}{\rm arcsec}\right)^{-0.85\pm0.02} {\rm K}, \quad (1)$$

$$T_{\rm kin}({\rm NH_3}) = 1057(\pm 119) \times \left(\frac{R}{\rm arcsec}\right)^{-0.68\pm0.02} {\rm K}, \quad (2)$$

with power-law indices of –0.85 and –0.68, respectively. The gas temperatures derived from H_2CO and NH_3 at projected distance are averaged within 12″ bins (∼0.12 pc) as shown in Fig. 5. Additionally, the average gas temperature data were fit, yielding fit results of

$$T_{\rm kin}({\rm H_2CO}) = 2788(\pm 1040) \times \left(\frac{R}{\rm arcsec}\right)^{-0.75\pm0.07} {\rm K}, \quad (3)$$

$$T_{\rm kin}({\rm NH_3}) = 1886(\pm 370) \times \left(\frac{R}{\rm arcsec}\right)^{-0.75\pm0.04} {\rm K}, \quad (4)$$

with the same power-law index of –0.75. These power-law indices are consistent with previous observations in various star formation regions, which typically range from -0.05 to -1.48 (e.g., Tang et al. 2018a; Gieser et al. 2019, 2021, 2022, 2023; Lin et al. 2022; Zhao et al. 2024), directly indicating that the dense gas in the PDR M17SW is heated by radiation emitted from OB star clusters in the cavity. These relations are based on the projected separation from the radiation source.

As the distance changes, the expected variation in gas temperature is predicted to adhere to the principles of the Stefan-Boltzmann blackbody radiation law ($T_{\rm kin} = 0.86 \times (\frac{L}{L_\odot})^{1/4}(\frac{R}{\rm pc})^{-1/2}$ K, where the luminosity, L, is given in terms of solar luminosity ($L_\odot$) and the distance, R, is measured in par-

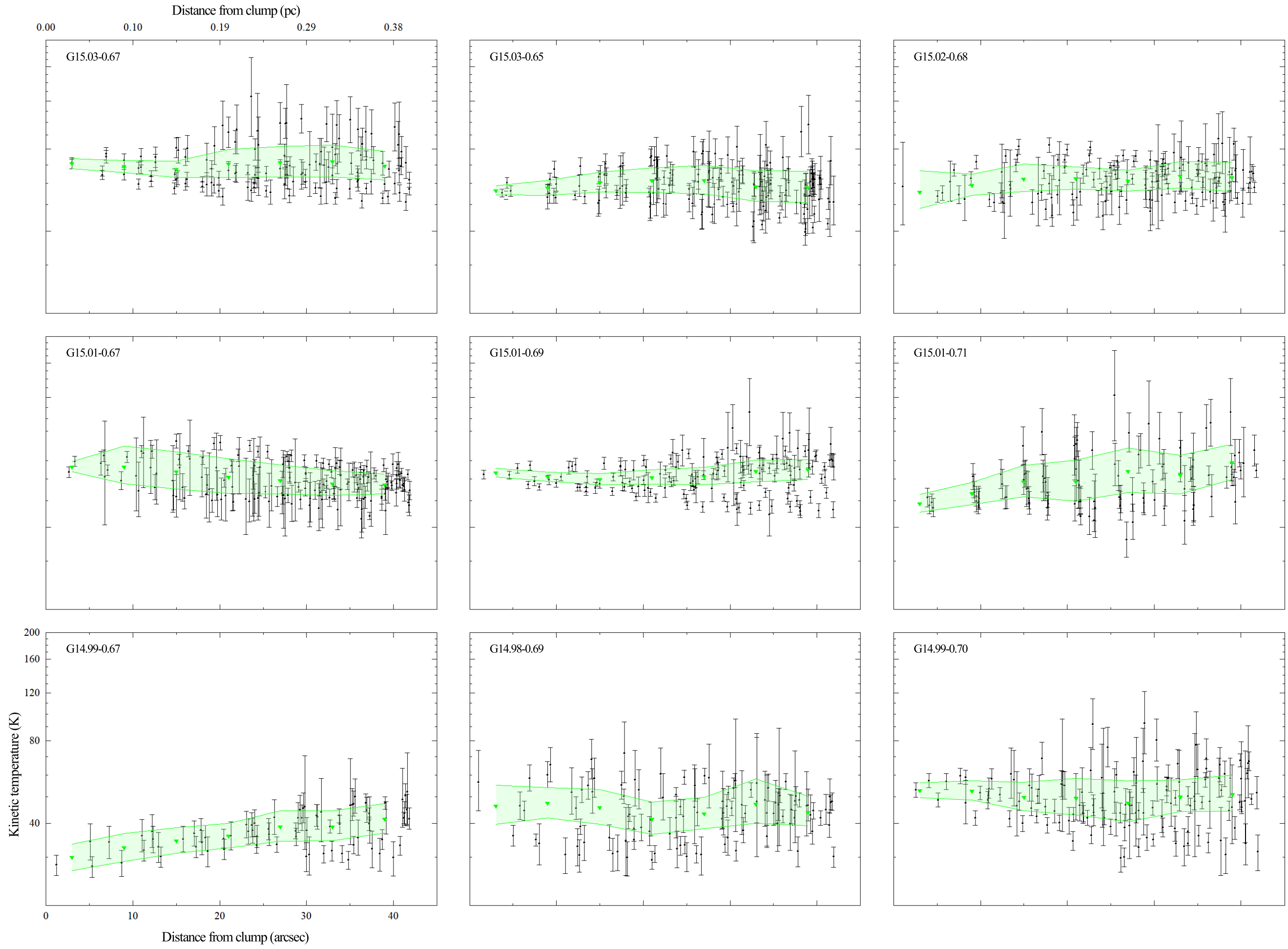

Fig. 6: Variations in the gas kinetic temperatures derived from H_2CO (3–2) line ratios, measured from the central regions of dense clumps (see Table 1) extending toward their respective peripheries. The green downward-pointing triangles represent the mean temperatures calculated in bins of 6″, with the shaded green areas indicating their uncertainties. The distances are plotted at the bin centers. To prevent cross-contamination from adjacent clumps, the data were restricted to the region on each clump's side of the midline between the two clumps.

secs). By refining the emissivity of dust grains to wavelengths below the characteristic blackbody temperature, the radiation law can be modified to $T_{\rm kin} = 2.7 \times (\frac{L}{L_\odot})^{1/5}(\frac{R}{\rm pc})^{-2/5}$ K (Wiseman & Ho 1998; Tang et al. 2018a). Considering the total luminosity estimated ranging from 4.5 to $5.6 \times 10^6\,L_\odot$ at a distance of 2.2 kpc (Povich et al. 2007), we adopt a representative value of $4 \times 10^6\,L_\odot$ for the M17 region at a distance of 2 kpc in this study. Our fit temperature result from H_2CO line ratios aligns with the modified Stefan-Boltzmann blackbody radiation law (see Fig. 5). However, the NH_3 data show better agreement with the Stefan-Boltzmann blackbody radiation law. Comparable results for H_2CO and NH_3 data were also observed in the OMC-1 region (Tang et al. 2018a). Similarly, the NH_3 data indicate two temperature components, "cold" and "warm," with distance from the cavity (see Fig. 5). The warm component corresponds to the results derived from H_2CO concerning distance, which closely matches the predicted outcomes from the modified Stefan-Boltzmann blackbody radiation law. Conversely, the cold component aligns with the predicted results from the unmodified Stefan-Boltzmann blackbody radiation law. Previous NH_3 observations have indicated the existence of both cold and warm gas components in M17SW (Güsten & Fiebig 1988). However, due to significant uncertainties in NH_3 data, a reliable and physically motivated separation of these components is not achievable. As a result, we retain a single-component analysis for deriving the temperature gradient from NH_3 data. Both radiation models for gas heating (Stefan-Boltzmann blackbody radiation and its modification related to dust emissivity) are well supported by our H_2CO and NH_3 data, making it challenging to discern which model is better.

In regions with distances of $R < 125''$ (∼1.25 pc) from the cavity, several locations exhibit gas temperatures probed with H_2CO and NH_3 above the fit results (see Fig. 5). Currently, extensive shocked gas surrounding the M17 H II region is detected on a large scale, likely originating from the collision between the expanding ionized gas and the ambient neutral medium (Zhu et al. 2023). The high temperatures of the dense gas near the M17 H II region may be attributed to shocks from the collisional interface and stellar winds from the H II region. For regions with $R = 160$–$240''$ (∼1.6–2.4 pc), some locations display gas temperatures probed with H_2CO and NH_3 above the fit results. These elevated temperatures are linked to dense gas structures in M17SW, particularly near dense clumps and H_2O and CH_3OH masers, suggesting that the dense gas may be heated by local star formation feedback such as radiation, outflows, shocks, and winds.

In addition to the distance from the cavity, we also examine the temperature gradient with respect to the assumed ionization front (see Fig. 4). Based on the morphology of the cloud and the spatial distribution of the UV radiation field, the ionization front is defined along the northeastern rim of M17SW. The orientation of the assumed ionization front was determined by performing principal component analysis on the spatial coordinates of the points along the southeastern edge of M17SW. The first principal component gives the direction of the edge, which we adopt as the orientation of the ionization front. The projected distance of each pixel to this front is then calculated. Fig. 5 shows the kinetic temperature as a function of distance from the assumed ionization front. A decreasing trend is clearly visible, with higher temperatures near the front and lower temperatures farther away.

We still performed power-law fits to the temperature–distance relations for both H_2CO and NH_3 to facilitate a qualitative comparison between the two tracers:

$$T_{\rm kin}({\rm H_2CO}) = 234(\pm13) \times \left(\frac{R}{\rm arcsec}\right)^{-0.34\pm0.01}\ {\rm K}, \quad (5)$$

$$T_{\rm kin}({\rm NH_3}) = 225(\pm11) \times \left(\frac{R}{\rm arcsec}\right)^{-0.43\pm0.01}\ {\rm K}, \quad (6)$$

with power-law indices of –0.34 and –0.43, respectively. We also averaged the gas temperatures obtained from H_2CO and NH_3 at projected distance within 12″ bins in Fig. 5. For the average gas temperature data, the fit results are

$$T_{\rm kin}({\rm H_2CO}) = 220(\pm28) \times \left(\frac{R}{\rm arcsec}\right)^{-0.32\pm0.03}\ {\rm K}, \quad (7)$$

$$T_{\rm kin}({\rm NH_3}) = 200(\pm31) \times \left(\frac{R}{\rm arcsec}\right)^{-0.38\pm0.03}\ {\rm K}, \quad (8)$$

with power-law indices of –0.32 and –0.38, respectively. These results are consistent with the scenario of external UV heating dominating the thermal balance in the M17SW region. One should note that the ionization front is defined from the cloud morphology rather than being directly observed, and projection effects are non-negligible. Accordingly, the fit temperature gradients should be interpreted with caution. Nevertheless, these fit results provide a meaningful comparison between H_2CO and NH_3, and the derived gradients are broadly consistent with predictions from the modified Stefan–Boltzmann blackbody radiation law.

To investigate the impact of internal radiation heating on the dense gas surrounding dense clumps within the M17SW region at a scale of 0.1–0.4 pc, we analyzed the temperature profiles of the nine dense clumps, already addressed in Table 1, in Fig. 6. Among these nine clumps, six (G15.03-0.67, G15.03-0.65, G15.02-0.68, G15.01-0.67, G14.98-0.69, and G14.99-0.70) are associated with maser emission (see Fig. 1), indicating ongoing star formation activities. G15.01-0.67 and G15.01-0.69 display weak temperature gradients that decrease with distance from the clump, suggesting that internal star formation activities may be responsible for heating the dense gas in these regions. In contrast, other dense clumps show no significant temperature gradient (that decrease with distance from the clump), possibly indicating that they are in an earlier evolutionary stage (such as Class I CH_3OH masers; Kurtz et al. 2004; Gómez et al. 2010; Kim et al. 2018a; Yang et al. 2020) with embedded protostars or clusters that have not yet generated sufficient heat to warm the surrounding molecular envelope significantly. The bolometric luminosities of four dense clumps, namely G15.03-0.67, G15.03-0.65, G15.01-0.67, and G15.01-0.71, have been measured by Urquhart et al. (2018) at values of 2.30, 1.25, 2.97, and 1.86×10^5 $L_\odot$, respectively. Assuming that the embedded young stellar objects (YSOs) or YSO candidates are the primary energy sources in these clumps based on the luminosity reported by Urquhart et al. (2018), gas temperatures derived from the modified Stefan-Boltzmann blackbody radiation law were found to be 74.5, 65.9, 78.4, and 71.4 K at radii of 0.12 pc, respectively, consistent with the 51–71 K range obtained from H_2CO line ratio measurements (see Table 1). At larger radii of 0.24 pc, the derived gas temperatures are 56.4, 50.0, 59.4, and 54.1 K, respectively, aligning with the typical temperature of 50–60 K derived from H_2CO in the M17SW region. These results suggest that the protostars and/or YSOs embedded within the cloud emit significant radiation, effectively heating the surrounding molecular gas. Therefore, internal radiation may play a substantial role in gas heating within the M17SW region on a small scale.

As previously discussed, the complex temperature structure of the M17SW region may be attributed to both large-scale external radiative heating and small-scale internal radiative heating. The presence of a significant gas temperature gradient across the M17SW region, as measured by H_2CO and NH_3, provides evidence that the dense gas is primarily heated by radiation emitted from OB star clusters within the cavity. On a smaller scale, the dense gas surrounding the dense clumps experiences significant heating from internal protostars and/or YSOs. However, the spatial resolution of our observations, approximately 0.12 pc, does not allow for a detailed measurement of the temperature structures within these dense clumps. Therefore, future high-resolution observations using ALMA will be necessary to overcome this limitation and provide a more comprehensive understanding of the temperature distribution in the region.

4.3. Turbulent heating

Previous observations of the M17SW region have revealed a complex velocity structure (Hobson 1992) with turbulence playing a significant role in broadening spectral lines (e.g., Güsten & Fiebig 1988; Pérez-Beaupuits et al. 2015; Hoang et al. 2022). Güsten & Fiebig (1988) found a strong correlation between local turbulence and gas temperature measured by NH_3 (1,1) and (2,2) lines on a scale of approximately 0.4 pc, indicating that dense gas in the M17SW region is heated by turbulence.

Our study also addresses the relationship between turbulence and kinetic temperature on a scale of unprecedented ~0.2 pc. To quantitatively analyze turbulence, we utilized the nonthermal line width ($\sigma_{\rm NT}$) of H_2CO. Positions with Mach numbers $\mathcal{M} \geq 4$, located near dense regions significantly impacted by nonthermal motions, were selected. The correlation between nonthermal line width and kinetic temperature for both H_2CO 3_{03}–2_{02} and the combined H_2CO 3_{22}–2_{21} and 3_{21}–2_{20} lines is depicted in Fig. 7. The correlation was fit with a power law, showing $T_{\rm kin} \propto \sigma_{\rm NT}^{0.47\pm0.06}$ for H_2CO 3_{03}–2_{02} and $T_{\rm kin} \propto \sigma_{\rm NT}^{0.55\pm0.04}$ for the combined H_2CO 3_{22}–2_{21} and 3_{21}–2_{20} lines. The correlation coefficients, r, were determined to be 0.30 and 0.52, respectively. These results suggest that the observed temperature increase in regions with strong nonthermal motions can be attributed to turbulent activities occurring on scales of ~0.2 pc, consistent with previous observational findings (Güsten & Fiebig 1988). The fit results of H_2CO 3_{03}–2_{02} and the combined H_2CO 3_{22}–2_{21} and 3_{21}–2_{20} lines in the M17SW region align with previous findings in the massive star-forming regions

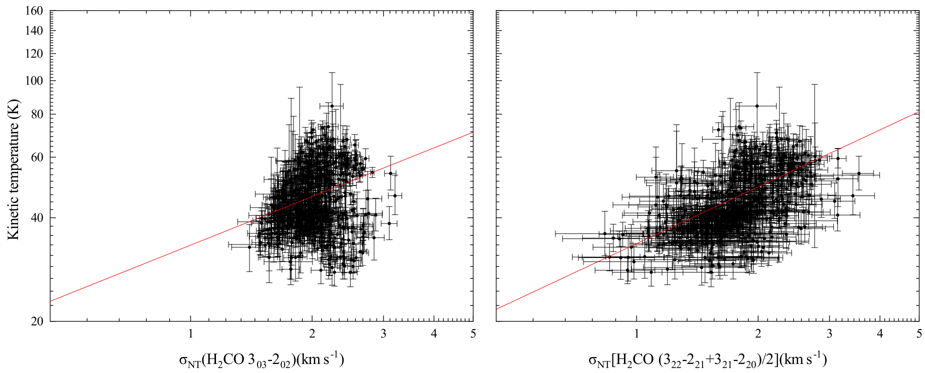

Fig. 7: Correlation between the non-thermal line width (σ_{NT}) and gas kinetic temperature (T_{kin}) obtained from the H_2CO line ratio is investigated in the M17SW region characterized by Mach numbers $\mathcal{M} \gtrsim 4.0$ (see Sect. 4.3). A linear regression analysis with weighting ($w = 1/\sigma^2$) is conducted on the H_2CO 3_{03}–2_{02} (*left*) and the combined H_2CO 3_{22}–2_{21} and 3_{21}–2_{20} (*right*) lines, resulting in: $\log T_{kin}$ = (0.47 ± 0.06) × $\log\sigma_{NT}$ + (1.52 ± 0.02) and $\log T_{kin}$ = (0.55 ± 0.04) × $\log\sigma_{NT}$ + (1.53 ± 0.01), respectively. The Pearson correlation coefficients (r) for these regressions (red lines) are 0.30 and 0.52, respectively.

OMC-1 and DR21 (Tang et al. 2018a; Zhao et al. 2024) and other massive clumps (ATLASGAL sample, Tang et al. 2018b) on scales ranging from 0.06 to 2 pc. The high-density environment of M17SW ($n(H_2) = 5.5\times10^5$ cm^{-3}) promotes rapid radiative cooling through atomic fine-structure lines such as [OI], [CI], and [CII], the latter having been previously detected in this region (Keene et al. 1985; Genzel et al. 1988; Stutzki et al. 1988; Pérez-Beaupuits et al. 2010). Consequently, the slightly lower power-law index of the H_2CO 3_{03}–2_{02} transition likely reflects a regime in which turbulent energy injection is largely balanced by efficient radiative cooling. While turbulence acts as a heating source, enhanced density contrasts and velocity gradients associated with turbulent motions may increase the effectiveness of line cooling, preventing a strong rise in gas temperature with increasing linewidth. As a result, the positive temperature–turbulence correlation observed in other star-forming regions is significantly weakened.

4.4. Comparison with the Orion Bar

Due to its proximity (~400 pc, Menten et al. 2007; Kounkel et al. 2017), the Orion Bar is recognized as one of the clearest PDRs of our Galaxy. Gas temperature structures within the Orion Bar have been elucidated through observations conducted using the APEX 12 m and IRAM 30 m telescopes, where the same H_2CO (3–2) lines were mapped at scales of approximately 0.06 and 0.024 pc, respectively (Leurini et al. 2010; Tang et al. 2018a). High temperatures ranging from 100 to 130 K are detected in the dense gas at the edge of the Orion Bar, while lower temperatures of around 73 K are observed within the internal dense clumps of the Orion Bar (Tang et al. 2018a). Notably, there is no evidence indicating massive star formation within the Orion Bar region. This may be attributed to its lower H_2 density and less effective shielding compared to M17SW, where denser gas and more efficient shielding create more favorable conditions for star formation. Gas heating in the Orion Bar is proposed to be primarily influenced by far ultraviolet (FUV) photons emitted from the Trapezium stars located in the northern H II region (Tang et al. 2018a). In contrast, the M17SW region exhibits prominent internal star formation activities, potentially leading to a more complex gas heating scenario in this region. On a larger scale, dense gas heating in the M17SW region may be significantly impacted by FUV photons originating from OB star clusters within the M17 cavity. Conversely, in smaller regions surrounding embedded protostars or clusters, dense gas heating likely results from a combination of processes including star formation activity, radiation, and turbulence, presenting a notable distinction from the conditions observed in the Orion Bar region.

4.5. Influence of star formation

Star formation can be triggered by feedback from newly born massive OB stars, a mechanism thoroughly explained by the radiation-driven implosion model. The skin of the molecular cloud is heated and ionized by the photoionizing radiation of the nearby OB stars, and the high pressure drives a reverse shock by the rocket effect that propagate through to the cool interior of the clumps (e.g., Dale & Bonnell 2012; Nakatani & Yoshida 2019). The FUV photons dissociate and heat the molecular gas, and affect the physics and chemistry of gas regulating star formation. FUV radiation may limit the final mass of the star through the photoevaporation of the outer layers of collapsing isothermal spheres which may rapidly deplete the envelope material, and trigger star formation with the compression of noncollapsing clumps by shock waves from the warm surface gas (Gorti & Hollenbach 2002). High gas temperature will affect the Jeans masses of dense cores (Jeans' mass $M_{Jeans} = 1.25 \times (\frac{T_{kin}}{10\,K})^{3/2} \times (\frac{n(H_2)}{10^5\,cm^{-3}})^{-1/2}$ M$_\odot$, where $n(H_2)$ is volume density and T_{kin} is the gas kinetic temperature) and may affect the initial mass function (IMF) of star formation. The Jeans mass is about 7 M$_\odot$ for the mean physical parameters of the molecular gas in M17SW ($T_{kin} \sim 54$ K and $n(H_2) \sim 5.5\times10^5$ cm^{-3}). The gas temperatures in M17SW exceed values found in typical Solar Neighborhood clouds ($T_{kin} \sim$ 10–16 K; e.g., Pineda et al. 2026) and infrared dark clouds ($T_{kin} \sim$ 10–20 K; e.g., Pillai et al. 2006; Chira et al. 2013) by a factor ~3–6, so that M_{Jeans} is lower by a factor ~4–13 in these clouds for fixed density $n(H_2)$. This indicates that the star-forming clumps in the M17SW region are massive (e.g., Urquhart et al. 2018; Eden et al. 2019), potentially facilitating the formation of high-mass stars and leading to a top-heavy IMF in the M17SW area.

5. Summary

The kinetic temperature structure of the PDR M17SW has been investigated with the H_2CO triplet ($J_{K_aK_c} = 3_{03}$–2_{02}, 3_{22}–2_{21}, and 3_{21}–2_{20}) transitions near 218 GHz on a linear scale of ~ 0.18 pc

(18″) with the IRAM 30 m telescope. The main results are the following:

1. The $H_2CO\ 3_{03}–2_{02}$ emission shows an extended distribution and reveals a clumpy structure of the dense gas in M17SW.
2. We determined the kinetic temperature by modeling the measured $H_2CO\ 0.5\times[(3_{22}–2_{21} + 3_{21}–2_{20})/3_{03}–2_{02}]$ line ratios with the RADEX non-LTE radiative transfer model. The derived kinetic temperatures ranges from 28 to 181 K with an average of 54.2 ± 0.3 K derived assuming a typical density of 5.5×10^5 cm^{-3}. In comparison to temperature measurements obtained from multiple transitions of NH_3 (1,1)–(6,6) and FIR wavelengths, which have lower angular resolution than H_2CO, the H_2CO lines exhibit temperatures similar to those measured by NH_3 but slightly higher than the values derived from FIR observations.
3. The kinetic temperature measurements using H_2CO indicate that the highest temperature ($T_{\rm kin}$>100 K) is associated with the ultracompact H II region UC1 and the eastern edge of M17SW. Elevated temperatures (>70 K) are observed at various locations including the eastern edge of the primary structure of M17SW, the edge of clump G15.01-0.71, clumps G15.03-0.67 and G14.99-0.70, southern regions of clumps G15.03-0.65, G15.02-0.68, G15.01-0.67, and G15.01-0.69, as well as in proximity to H_2O and CH_3OH masers. Moderate temperatures ranging from 50 to 70 K are commonly found in the periphery of the primary structure of M17SW. Lower temperatures (<50 K) are identified at the western edge of M17SW and the edges of clumps G15.01-0.71 and G14.99-0.70.
4. The temperature gradient within the M17SW region as indicated by the H_2CO (3–2) and NH_3 (2,2)/(1,1) line ratios indicates that the dense gas in M17SW is strongly affected by the radiation emitted from the OB star cluster NGC 6618 in the cavity with temperatures decreasing from northeast to southwest.
5. On a smaller scale, the protostars and/or YSOs embedded within the cloud emit substantial radiation, which effectively heats the surrounding molecular gas. This internal radiation likely plays a significant role in the heating of dense gas within the M17SW region.
6. The nonthermal line widths of H_2CO exhibit a correlation with the gas kinetic temperatures in the M17SW region, which indicates that higher temperatures measured by H_2CO are linked to turbulence on a scale of ~0.2 pc.

The kinetic temperature of the molecular gas is a fundamental parameter in our attempts to comprehend the ISM. M17SW serves as an optimal location to investigate the ISM and star formation within dense PDRs. Future studies with high-resolution observations will concentrate on this region to further utilize formaldehyde as a thermometer, enhancing our understanding of gas heating and its effects on the star formation process.

Acknowledgements. The authors thank the anonymous referee for helpful comments. We thank the staff of the IRAM telescope for their assistance in observations. This work acknowledges the support of the National Key R&D Program of China under grant Nos. 2023YFA1608002 and 2022YFA1603103, the Chinese Academy of Sciences (CAS) "Light of West China" Program under grant No. xbzg-zdsys-202212, and the Tianshan Talent Training Program of Xinjiang Uygur Autonomous Region under grant Nos. 2022TSYCLJ0005. It was also partially supported by the Tianshan Talent Training Program of Xinjiang Uygur Autonomous Region under grant No. 2024TSYCTD0013, the National Natural Science Foundation of China under grant Nos. 12173075, 12373029, 12403033, and 12463006, the Xinjiang Key Laboratory of Radio Astrophysics under grant No. 2023D04033, the Natural Science Foundation of Xinjiang Uygur Autonomous Region under grant Nos. 2022D01A359 and 2023D01A11, the Central Guidance for Local Science and Technology Development Fund under grant No. ZYYD2025ZY23, and the Youth Innovation Promotion Association CAS. C. Henkel acknowledges support by the Chinese Academy of Sciences President's International Fellowship Initiative under grant No. 2025PVA0048. T. Liu, K. Wang, X. P. Chen, and J. W. Wu acknowledge support by the Tianchi Talent Program of Xinjiang Uygur Autonomous Region. This research has used NASA's Astrophysical Data System (ADS).

References

Ao, Y., Henkel, C., Menten, K. M., et al. 2013, A&A, 550, A135
Bakes, E. L. O. & Tielens, A. G. G. M. 1994, ApJ, 427, 822
Beetz, M., Elsaesser, H., Weinberger, R., & Poulakos, C. 1976, A&A, 50, 41
Bergin, E. A., Goldsmith, P. F., Snell, R. L., & Ungerechts, H. 1994, ApJ, 431, 674
Beuther, H., Kuiper, R., & Tafalla, M. 2025, ARA&A, 63, 1
Breen, S. L., Caswell, J. L., Ellingsen, S. P., & Phillips, C. J. 2010, MNRAS, 406, 1487
Breen, S. L. & Ellingsen, S. P. 2011, MNRAS, 416, 178
Brogan, C. L. & Troland, T. H. 2001, ApJ, 560, 821
Busquet, G., Estalella, R., Palau, A., et al. 2016, ApJ, 819, 139
Caselli, P., Hasegawa, T. I., & Herbst, E. 1993, ApJ, 408, 548
Chen, Z., Jiang, Z., Wang, Y., et al. 2012, PASJ, 64, 110
Chen, Z., Johnstone, D., Contreras Peña, C., et al. 2025, AJ, 170, 125
Chen, Z., Nürnberger, D. E. A., Chini, R., et al. 2013, A&A, 557, A51
Chen, Z., Sun, W., Chini, R., et al. 2021, ApJ, 922, 90
Chini, R., Elsaesser, H., & Neckel, T. 1980, A&A, 91, 186
Chini, R., Nielbock, M., & Beck, R. 2000, A&A, 357, L33
Chira, R.-A., Beuther, H., Linz, H., et al. 2013, A&A, 552, A40
Cuadrado, S., Goicoechea, J. R., Cernicharo, J., et al. 2017, A&A, 603, A124
Dale, J. E. & Bonnell, I. A. 2012, MNRAS, 422, 1352
Dewangan, L. K., Ojha, D. K., Luna, A., et al. 2016, ApJ, 819, 66
Dupac, X., Giard, M., Bernard, J. P., et al. 2002, A&A, 392, 691
Eden, D. J., Liu, T., Kim, K.-T., et al. 2019, MNRAS, 485, 2895
Elmegreen, B. G. & Lada, C. J. 1977, ApJ, 214, 725
Felli, M., Churchwell, E., & Massi, M. 1984, A&A, 136, 53
Forster, J. R. & Caswell, J. L. 1999, A&AS, 137, 43
Gardner, F. F. & Whiteoak, J. B. 1981, PASA, 4, 240
Gatley, I., Becklin, E. E., Sellgren, K., & Werner, M. W. 1979, ApJ, 233, 575
Genzel, R., Harris, A. I., Jaffe, D. T., & Stutzki, J. 1988, ApJ, 332, 1049
Gerner, T., Beuther, H., Semenov, D., et al. 2014, A&A, 563, A97
Gieser, C., Beuther, H., Semenov, D., et al. 2023, A&A, 674, A160
Gieser, C., Beuther, H., Semenov, D., et al. 2021, A&A, 648, A66
Gieser, C., Beuther, H., Semenov, D., et al. 2022, A&A, 657, A3
Gieser, C., Semenov, D., Beuther, H., et al. 2019, A&A, 631, A142
Ginsburg, A., Darling, J., Battersby, C., Zeiger, B., & Bally, J. 2011, ApJ, 736, 149
Ginsburg, A., Henkel, C., Ao, Y., et al. 2016, A&A, 586, A50
Girichidis, P., Offner, S. S. R., Kritsuk, A. G., et al. 2020, Space Sci. Rev., 216, 68
Gómez, L., Luis, L., Hernández-Curiel, I., et al. 2010, ApJS, 191, 207
Gong, Y., Ortiz-León, G. N., Rugel, M. R., et al. 2023, A&A, 678, A130
Gong, Y., Zhang, Z.-y., Henkel, C., et al. 2025, ApJ, 994, 158
Gong, Y., Zhong, J., Ren, Y., et al. 2026, Science Advances, 12, 1.9433
Gorti, U. & Hollenbach, D. 2002, ApJ, 573, 215
Greaves, J. S., White, G. J., & Williams, P. G. 1992, A&A, 257, 731
Güsten, R. & Fiebig, D. 1988, A&A, 204, 253
Guzmán, V., Pety, J., Goicoechea, J. R., Gerin, M., & Roueff, E. 2011, A&A, 534, A49
Hanson, M. M., Howarth, I. D., & Conti, P. S. 1997, ApJ, 489, 698
Harris, A. I., Stutzki, J., Genzel, R., et al. 1987, ApJ, 322, L49
Heikkilä, A., Johansson, L. E. B., & Olofsson, H. 1999, A&A, 344, 817
Henkel, C., Hunt, L. K., & Izotov, Y. I. 2022, Galaxies, 10, 11
Henkel, C., Walmsley, C. M., & Wilson, T. L. 1980, A&A, 82, 41
Henkel, C., Wilson, T. L., Walmsley, C. M., & Pauls, T. 1983, A&A, 127, 388
Hernández-Vera, C., Guzmán, V. V., Goicoechea, J. R., et al. 2023, A&A, 677, A152
Hoang, T. D., Ngoc, N. B., Diep, P. N., et al. 2022, ApJ, 929, 27
Hobson, M. P. 1992, MNRAS, 256, 457
Hobson, M. P., Padman, R., Scott, P. F., Prestage, R. M., & Ward-Thompson, D. 1993, MNRAS, 264, 1025
Hoffmeister, V. H., Chini, R., Scheyda, C. M., et al. 2006, A&A, 457, L29
Hoffmeister, V. H., Chini, R., Scheyda, C. M., et al. 2008, ApJ, 686, 310
Hollenbach, D. J., Takahashi, T., & Tielens, A. G. G. M. 1991, ApJ, 377, 192
Howe, J. E., Ashby, M. L. N., Bergin, E. A., et al. 2000, ApJ, 539, L137
Immer, K., Kauffmann, J., Pillai, T., Ginsburg, A., & Menten, K. M. 2016, A&A, 595, A94
Jaffe, D. T., Harris, A. I., & Genzel, R. 1987, ApJ, 316, 231

Jiang, Z., Yao, Y., Yang, J., et al. 2002, ApJ, 577, 245
Johnston, K. G., Beuther, H., Linz, H., et al. 2014, A&A, 568, A56
Johnstone, D., Boonman, A. M. S., & van Dishoeck, E. F. 2003, A&A, 412, 157
Kahle, K. A., Hernández-Gómez, A., Wyrowski, F., & Menten, K. M. 2023, A&A, 673, A143
Kahle, K. A., Wyrowski, F., König, C., et al. 2024, A&A, 687, A162
Keene, J., Blake, G. A., Phillips, T. G., Huggins, P. J., & Beichman, C. A. 1985, ApJ, 299, 967
Kennicutt, Robert C., J. 1998a, ARA&A, 36, 189
Kennicutt, Robert C., J. 1998b, ApJ, 498, 541
Keown, J., Di Francesco, J., Rosolowsky, E., et al. 2019, ApJ, 884, 4
Khan, S., Jacob, A. M., Rugel, M. R., et al. 2026, A&A, 706, A280
Kim, C.-H., Kim, K.-T., & Park, Y.-S. 2018a, ApJS, 236, 31
Kim, J.-G., Kim, W.-T., & Ostriker, E. C. 2018b, ApJ, 859, 68
Klessen, R. S., Spaans, M., & Jappsen, A.-K. 2007, MNRAS, 374, L29
Kounkel, M., Hartmann, L., Loinard, L., et al. 2017, ApJ, 834, 142
Kurtz, S., Hofner, P., & Álvarez, C. V. 2004, ApJS, 155, 149
Lada, C. & Chaisson, E. J. 1975, ApJ, 195, 367
Lada, C., Dickinson, D. F., & Penfield, H. 1974, ApJ, 189, L35
Lada, C. J. 1976, ApJS, 32, 603
Lada, C. J., Depoy, D. L., Merrill, K. M., & Gatley, I. 1991, ApJ, 374, 533
Lemke, D. & Harris, A. W. 1981, A&A, 99, 285
Leurini, S., Parise, B., Schilke, P., Pety, J., & Rolffs, R. 2010, A&A, 511, A82
Lim, W., De Buizer, J. M., & Radomski, J. T. 2020, ApJ, 888, 98
Lin, Y., Wyrowski, F., Liu, H. B., et al. 2022, A&A, 658, A128
Liu, B., Yang, R.-z., & Chen, Z. 2022, MNRAS, 513, 4747
Liu, H.-L., Sanhueza, P., Liu, T., et al. 2020, ApJ, 901, 31
Lu, X., Zhang, Q., Kauffmann, J., et al. 2017, ApJ, 839, 1
Luisi, M., Anderson, L. D., Schneider, N., et al. 2021, Science Advances, 7, eabe9511
Mangum, J. G., Darling, J., Henkel, C., & Menten, K. M. 2013, ApJ, 766, 108
Mangum, J. G., Darling, J., Menten, K. M., & Henkel, C. 2008, ApJ, 673, 832
Mangum, J. G., Ginsburg, A. G., Henkel, C., et al. 2019, ApJ, 871, 170
Mangum, J. G. & Wootten, A. 1993, ApJS, 89, 123
Mangum, J. G., Wootten, A., Loren, R. B., & Wadiak, E. J. 1990, ApJ, 348, 542
Mazumdar, P., Tram, L. N., Wyrowski, F., Menten, K. M., & Tang, X. 2022, A&A, 668, A180
Meixner, M., Haas, M. R., Tielens, A. G. G. M., Erickson, E. F., & Werner, M. 1992, ApJ, 390, 499
Menten, K. M., Reid, M. J., Forbrich, J., & Brunthaler, A. 2007, A&A, 474, 515
Mühle, S., Seaquist, E. R., & Henkel, C. 2007, ApJ, 671, 1579
Mundy, L. G., Evans, Neal J., I., Snell, R. L., & Goldsmith, P. F. 1987, ApJ, 318, 392
Mundy, L. G., Snell, R. L., Evans, Neal J., I., Goldsmith, P. F., & Bally, J. 1986, ApJ, 306, 670
Nakatani, R. & Yoshida, N. 2019, ApJ, 883, 127
Nielbock, M., Chini, R., Jütte, M., & Manthey, E. 2001, A&A, 377, 273
Nishimura, A., Minamidani, T., Umemoto, T., et al. 2018, PASJ, 70, S42
Pabst, C., Higgins, R., Goicoechea, J. R., et al. 2019, Nature, 565, 618
Pan, L. & Padoan, P. 2009, ApJ, 692, 594
Papadopoulos, P. P., Thi, W.-F., Miniati, F., & Viti, S. 2011, MNRAS, 414, 1705
Paumard, T., Genzel, R., Martins, F., et al. 2006, ApJ, 643, 1011
Pellegrini, E. W., Baldwin, J. A., Brogan, C. L., et al. 2007, ApJ, 658, 1119
Pérez-Beaupuits, J. P., Güsten, R., Spaans, M., et al. 2015, A&A, 583, A107
Pérez-Beaupuits, J. P., Spaans, M., Hogerheijde, M. R., et al. 2010, A&A, 510, A87
Pérez-Beaupuits, J. P., Wiesemeyer, H., Ossenkopf, V., et al. 2012, A&A, 542, L13
Pillai, T., Wyrowski, F., Carey, S. J., & Menten, K. M. 2006, A&A, 450, 569
Pineda, J. E., Friesen, R. K., Rosolowsky, E., et al. 2026, ApJS, 282, 18
Povich, M. S., Stone, J. M., Churchwell, E., et al. 2007, ApJ, 660, 346
Qin, S.-L., Zhao, J.-H., Moran, J. M., et al. 2008, ApJ, 677, 353
Reid, M. A. & Wilson, C. D. 2006, ApJ, 644, 990
Schuster, K. F., Boucher, C., Brunswig, W., et al. 2004, A&A, 423, 1171
Shirley, Y. L. 2015, PASP, 127, 299
Snell, R. L., Howe, J. E., Ashby, M. L. N., et al. 2000, ApJ, 539, L97
Stutzki, J. & Güsten, R. 1990, ApJ, 356, 513
Stutzki, J., Stacey, G. J., Genzel, R., et al. 1988, ApJ, 332, 379
Tang, X. D., Esimbek, J., Zhou, J. J., et al. 2013, A&A, 551, A28
Tang, X.-D., Esimbek, J., Zhou, J.-J., Wu, G., & Okoh, D. 2014, Research in Astronomy and Astrophysics, 14, 959
Tang, X. D., Henkel, C., Chen, C. H. R., et al. 2017a, A&A, 600, A16
Tang, X. D., Henkel, C., Menten, K. M., et al. 2021, A&A, 655, A12
Tang, X. D., Henkel, C., Menten, K. M., et al. 2019, A&A, 629, A6
Tang, X. D., Henkel, C., Menten, K. M., et al. 2018a, A&A, 609, A16
Tang, X. D., Henkel, C., Menten, K. M., et al. 2017b, A&A, 598, A30
Tang, X. D., Henkel, C., Wyrowski, F., et al. 2018b, A&A, 611, A6
Thronson, H. A., J. & Lada, C. J. 1983, ApJ, 269, 175
Tobin, J. J., Sheehan, P. D., Reynolds, N., et al. 2020, ApJ, 905, 162
Townsley, L. K., Feigelson, E. D., Montmerle, T., et al. 2003, ApJ, 593, 874
Urquhart, J. S., König, C., Giannetti, A., et al. 2018, MNRAS, 473, 1059
Urquhart, J. S., Morgan, L. K., Figura, C. C., et al. 2011, MNRAS, 418, 1689
van der Tak, F. F. S., Black, J. H., Schöier, F. L., Jansen, D. J., & van Dishoeck, E. F. 2007, A&A, 468, 627
van 't Hoff, M. L. R., Tobin, J. J., Harsono, D., & van Dishoeck, E. F. 2018, A&A, 615, A83
Walch, S. K., Whitworth, A. P., Bisbas, T., Wünsch, R., & Hubber, D. 2012, MNRAS, 427, 625
Wang, M., Chin, Y. N., Henkel, C., Whiteoak, J. B., & Cunningham, M. 2009, ApJ, 690, 580
Wang, Y., Jaffe, D. T., Evans, Neal J., I., et al. 1993, ApJ, 419, 707
Weingartner, J. C. & Draine, B. T. 2001, ApJS, 134, 263
Wiesenfeld, L. & Faure, A. 2013, MNRAS, 432, 2573
Wilson, C. D., Howe, J. E., & Balogh, M. L. 1999, ApJ, 517, 174
Wiseman, J. J. & Ho, P. T. P. 1998, ApJ, 502, 676
Xu, Y., Moscadelli, L., Reid, M. J., et al. 2011, ApJ, 733, 25
Yang, W., Gong, Y., Menten, K. M., et al. 2023, A&A, 675, A112
Yang, W., Xu, Y., Choi, Y. K., et al. 2020, ApJS, 248, 18
Yanza, V., Masqué, J. M., Dzib, S. A., et al. 2022, AJ, 163, 276
Yin, J., Chen, Z., Yao, Y., et al. 2022, Research in Astronomy and Astrophysics, 22, 035021
Yue, Z., Ao, Y., Tang, X., et al. 2026, ApJ, 1002, 77
Zhang, Z., Lu, X., Liu, T., et al. 2025, ApJ, 980, 44
Zhang, Z.-Y., Romano, D., Ivison, R. J., Papadopoulos, P. P., & Matteucci, F. 2018, Nature, 558, 260
Zhao, M., Qiu, K., Kang, J.-h., et al. 2026, ApJ, 1005, 91
Zhao, X., Tang, X. D., Henkel, C., et al. 2024, A&A, 687, A207
Zhou, W., Chen, Z., Jiang, Z., Feng, H., & Jiang, Y. 2024, ApJ, 969, L6
Zhu, F.-Y., Wang, J., Yan, Y., Zhu, Q.-F., & Li, J. 2023, MNRAS, 522, 503

Appendix A: Previous measurements of temperature in M17SW region

Based on previous observations of low-J transitions of ^{12}CO, ^{13}CO, and CH_3CCH, the temperature in the M17SW cloud core has been estimated to be between 50 and 60 K (e.g., Bergin et al. 1994; Wilson et al. 1999; Howe et al. 2000; Snell et al. 2000). In contrast, the mean temperature of the overall cloud is approximately 30 to 35 K. Observations of mid- to high-J ^{12}CO transitions reveal the presence of warmer gas in the M17SW region (e.g., Harris et al. 1987; Stutzki et al. 1988; Pérez-Beaupuits et al. 2010). The kinetic temperature of the warm dense gas ($n(H_2) \gtrsim 10^4$ cm^{-3}) is found to be at least 100 K. A non-LTE estimate of the ambient conditions indicates that the high-density clumps (with densities around $5{\times}10^5$ cm^{-3}) have temperatures of $\lesssim$230 K (Pérez-Beaupuits et al. 2010). In contrast, temperatures in the interface between the molecular cloud and the H II region range from 200 to 500 K. Güsten & Fiebig (1988) utilized the Effelsberg 100 m telescope (beam size ~ 40″) to map the temperature structure of the M17SW region with multiple transitions of NH_3 (1,1)–(6,6). Their results indicate that temperatures within the M17SW molecular cloud range from ~30 to 275 K, with a bulk temperature around 50 K. The kinetic temperature decreases gradually to about 30 K as one moves away from the radiating surface. Subsequent mapping of the M17SW molecular cloud was conducted using the Green Bank Telescope (GBT), focusing on the NH_3 (1,1) and (2,2) lines (beam size ~ 32″; Keown et al. 2019). The kinetic temperature in M17SW was measured using the line ratios of the NH_3 (1,1) and (2,2) transitions, revealing a range of 20–>80 K, with an average of ~40 K. These measurements of gas temperature in M17SW are listed in Table A.1.

The dust temperature structure of the M17SW region has been estimated in the wavelength range of 30 to 850 μm (e.g., Gatley et al. 1979; Meixner et al. 1992; Dupac et al. 2002; Hoang et al. 2022). The analysis indicates that the dust temperature varies uniformly across the M17SW region. Using the dust emission from 30 and 100 μm, Gatley et al. (1979) derived a color temperature map showing that temperatures in the M17SW cloud decrease from over 120 K to below 50 K as the distance from the H II region increases. Dupac et al. (2002) measured the dust temperature using emission data from 200 to 580 μm, revealing that temperatures exceeding 80 K (around 100 K or higher) in regions near the ionization front, while T_{dust} is 29 K at the intensity peak of M17SW. Additionally, Hoang et al. (2022) measured the dust temperature utilizing *Herschel* data from 160 to 500 μm and SCUBA2 data at 850 μm. Their dust temperature map shows a decrease from over 63 K at the northeast edge to below 30 K at the southwest edge of M17SW, also emphasizing a gradient in dust temperature consistent with that reported by Dupac et al. (2002). These measurements of dust temperature in M17SW are detailed in Table A.1.

Table A.1: Previous measurements of temperature in M17SW.

Molecule/ wavelength	Telescope	Beam size ″	T(range) K	T(average) K	References
NH_3 (1,1)–(6,6)	Effelsberg 100m	40	30–275	~50	Güsten & Fiebig (1988)
^{12}CO 1–0	FCRAO 14m	45	26–62	48	Bergin et al. (1994)
CH_3CCH 6–5	FCRAO 14m	50	25–52	34	Bergin et al. (1994)
^{13}CO 1–0 & 5–4	FCRAO 14m & SWAS	47 & 240	20–63	35	Howe et al. (2000)
^{12}CO 7–6 & 6–5	APEX	7.7	40–$\lesssim$230	...	Pérez-Beaupuits et al. (2010)
NH_3 (1,1)–(2,2)	GBT	32	20–>80	~40	Keown et al. (2019)
30, 50, 100 μm	KAO	60	50–100	...	Gatley et al. (1979)
50, 100 μm	KAO	30 & 40	<40–>75	...	Meixner et al. (1992)
200, 260, 360, 580 μm	PRONAOS	210	10–>80	...	Dupac et al. (2002)
160, 250, 350, 500 μm	*Herschel*	36	<30–>63	~43	Hoang et al. (2022)

Appendix B: H_2CO velocity channel maps

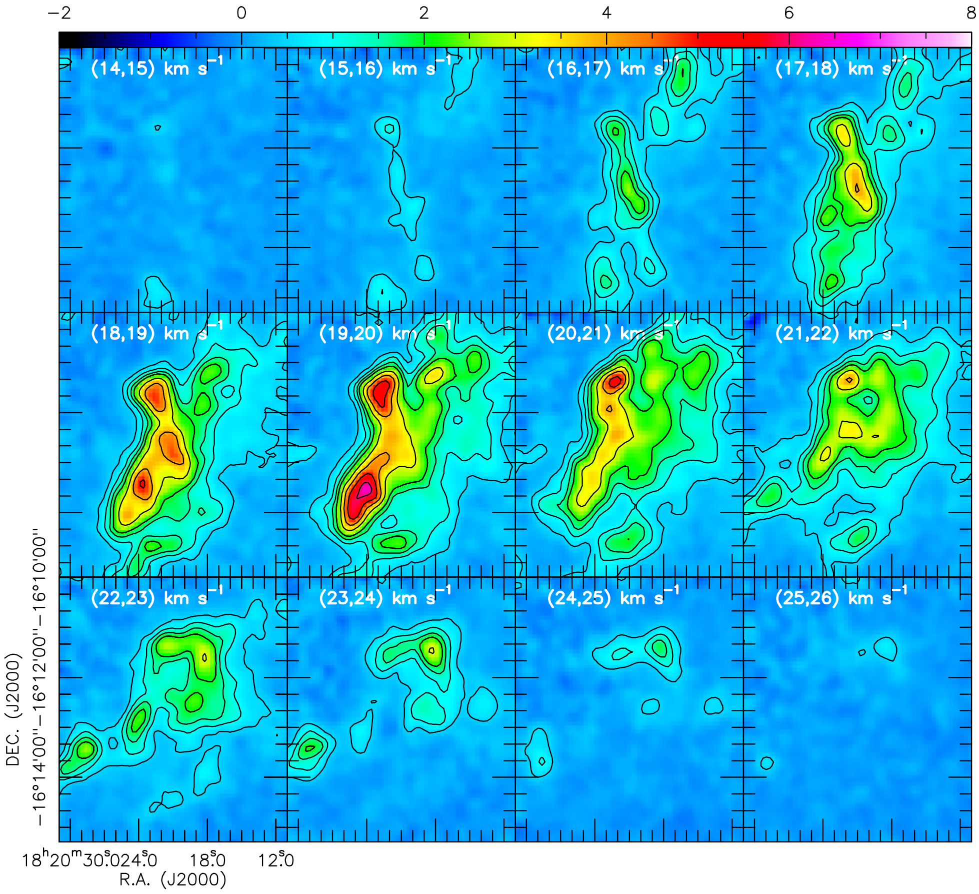

Fig. B.1: Channel maps of the $H_2CO\,(3_{03}–2_{02})$ transition. The contour levels are running from 0.5 to 2.0 K km s^{-1} in steps of 0.5 K km s^{-1} and from 2 to 8 K km s^{-1} in steps of 1 K km s^{-1} ($T_{\rm mb}$ scale; color bar in units of Kelvin kilometers per second).

Appendix C: The LTE and non-LTE models for H_2CO and NH_3 temperature map

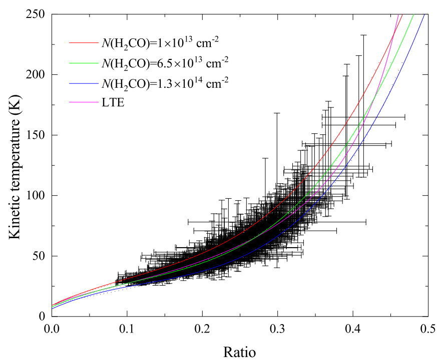

Fig. C.1: The relation between the kinetic temperature and the average ratio of $H_2CO\,3_{22}–2_{21}/3_{03}–2_{02}$ and $3_{21}–2_{20}/3_{03}–2_{02}$ modeled by RADEX non-LTE with an assumed density of $n(H_2) = 5.5\times10^5$ cm^{-3}, column densities N(para-H_2CO) = 1.0×10^{13}, 6.5×10^{13} and 1.3×10^{14} cm^{-2} (*red*, *green*, and *blue*), and an averaged linewidth of 3.8 km s^{-1}. The LTE kinetic temperature ($T_{\rm LTE}$, *magenta*) is calculated as $T_{\rm LTE} = \frac{47.1}{\ln(0.556/\mathrm{ratio})}$ K (where the ratio represents the average ratio of $H_2CO\,3_{22}–2_{21}/3_{03}–2_{02}$ and $3_{21}–2_{20}/3_{03}–2_{02}$) using the methodology described in Mangum & Wootten (1993) and Tang et al. (2017b). The black points were derived from observed H_2CO line ratios in the M17SW region for a column density N(para-H_2CO) = 6.5×10^{13} cm^{-2}. Temperature uncertainties were determined based on observed H_2CO line ratio errors.

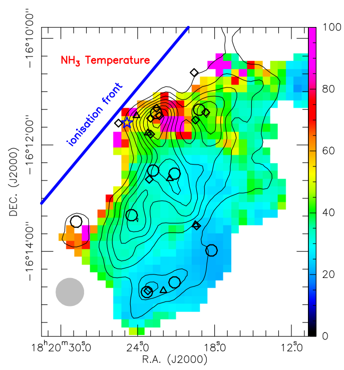

Fig. C.2: Map of the kinetic temperatures obtained from NH_3 (2,2)/(1,1) line ratios observed with the GBT (also see Fig.11 in Keown et al. 2019), represented by the color bar in units of Kelvin. Black contours show the integrated intensity of $H_2CO\,3_{03}–2_{02}$ (same as in Fig. 1). The marks are the same as in Fig. 1. The beam size of the NH_3 data is shown in the lower left corner. The solid blue line indicates the location of the assumed ionization front.